INTEGRATING REMOTE SENSING AND INFILTRATION MODEL TO ANALYZE THE PONDING DYNAMICS IN HUNGARY
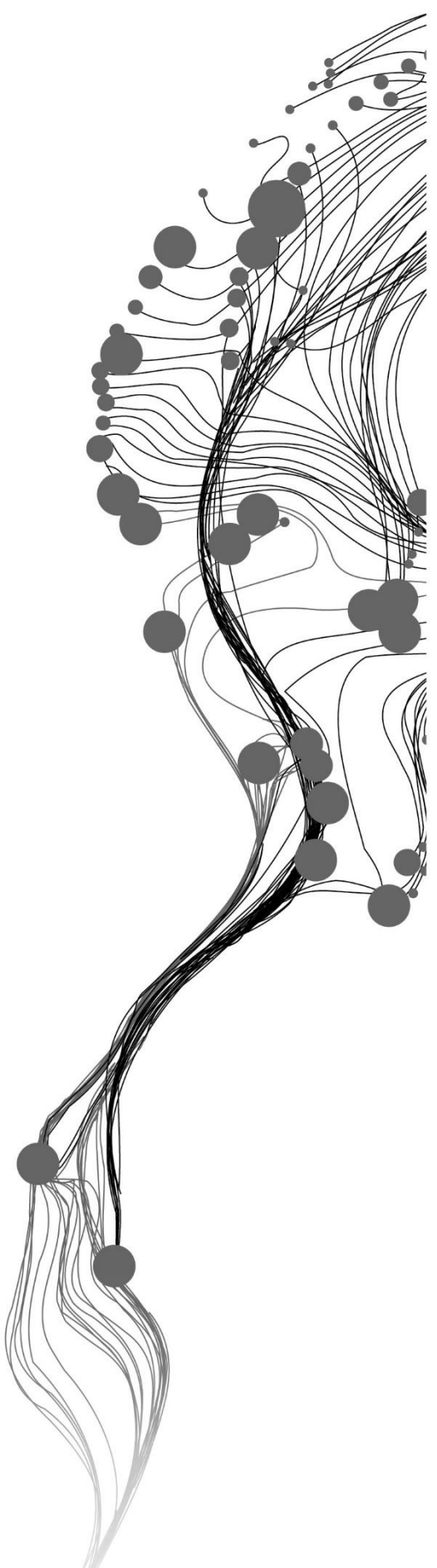
ANITA KHADKA

February, 2018

SUPERVISORS:

Dr Zoltán Vekerdy

Ir Arno van Lieshout

Integrating Remote Sensing and Infiltration Model to Analyze the Ponding Dynamics in Hungary

ANITA KHADKA

Enschede, The Netherlands, August 2018

SUPERVISORS:
Dr. Zoltán Vekerdy
Ir. Arno van Lieshout

THESIS ASSESSMENT BOARD:
Dr. M.W. Lubczynski (Chair)
Dr. Ir. D.C.M. Augustijn (External Examiner, University of Twente)

ABSTRACT

Ponding excess water caused by low runoff, insufficient evaporation, and low infiltration capacity of soil or by upwelling of groundwater is a nuisance in agricultural lands of Hungary. Mapping the location, extent, timing, and severity of excess water inundation with spatial and temporal resolution dataset has been in progress to plan adaptive and preventive measures. Different properties of soil in the agricultural lands of Hungary has been recognized as one of the causal factor promoting the formation of ponding. In this regard, this research focused to describe the dynamics of ponding excess water on agricultural fields based on modelling the infiltration process using data from satellite images and field observations. Comparative analysis was carried out considering the ponding and non-ponding location. Soil physical properties such as particle size, bulk density, porosity, organic carbon, and saturated hydraulic conductivity were determined based on laboratory work, and hydraulic parameters were derived using different pedo-transfer functions. Satellite data was processed to analyse the timing of ponding in the area. HYDRUS-1D model was established in heterogeneous profile of ponding (310 cm) and non-ponding location (250 cm) to simulate the process of soil water infiltration at five selected dephts. Field measured water content data was used to calibrate the model for the period of 25th September-5th December 2018. Calibrated model was used to simulate ponding based on soil hydraulic parameters of two kinds for the period of 1st January to 28th March, 2016. Model simulated ponding was validated with satellite detected ponding during the study period.

Ponding and non-ponding location was predominantly characterized by heavy clay and silty clay respectively for a good length of one meters deep soil profile. Increasing bulk density and decreasing organic matter content was measured with increasing depth. Calibrated model showed a reasonable level of accuracy with an average RMSE of 0.018 cm^3/cm^3, d-index of 0.638 and RVE of -2.83%. Because of error in experimental set up of sensors installed in the field high level of accuracy could not be achieved. Compared to satellite data, HYDRUS was fairly able to simulate ponding timing and duration. Simulated infiltration rates in ponding location were half the ones measured in non-ponding location. Measured clayey texture was attributed to very less infiltration and thus reason for ponding development. It can be concluded that the calibrated model though was capable of simulating ponding dynamics in the study site, it further requires refinement and needs to be tested by using volumes calculated from high resolution digital elevation model.

Keywords: Ponding excess water, soil physical properties, infiltration, HYDRUS, calibration

ACKNOWLEDGEMENTS

TABLE OF CONTENTS

LIST OF FIGURES

LIST OF TABLES

LIST OF ANNEX

ACRONYMS

ANN	Artificial Neural Network
BD	Bulk Density
DEM	Digital Elevation Model
DSS	Disturbed Soil Sample
ECMWF	European Centre for Medium-Range Weather Forecasts
ET	Evapotranspiration
GIS	Geographic Information System
GRD	Ground Range Detected
GW	Ground Water
HYPRES	Hydraulic Properties of European Soils
ISRIC	International Soil Reference and Information Centre
ISWC	Initial Soil Water Content
K_{sat}	Saturated Hydraulic Conductivity
LAI	Leaf Area Index
MAE	Mean Absolute Error
ME	Mean Error
NDVI	Normalized Difference Value Index
NPEW	Non-Ponding Excess Water
OC	Organic Carbon
OM	Organic Matter
PCP	Precipitation
PEW	Ponding Excess Water
PSD	Particle Size Distribution
PTF	Pedo-transfer Function
RMSE	Root Mean Square Error
RVE	Relative Volume Error
RWU	Root Water Uptake
SG	Soil Grids
SHP	Soil Hydraulic Parameter
SM	Soil Moisture
SPP	Soil Physical Property
SSWC	Saturated Soil Water Content
SWC	Soil Water Content
SWC	Soil Water Content
TM	Thematic Mapper
UDSS	Undisturbed Soil Sample
USDA	United Stated Department of Agriculture
VG	Van Genuchten
VWC	Volumetric Water Content
WB	Water Balance
XRCT	X-ray computer tomography
XRPD	X-ray powder diffraction

1.   INTRODUCTION

1.1.   Background

Ponding excess water (PEW), also commonly known as inland excess water or areal flood or surface water flood (van Leeuwen, Pravetz, Liptay, & Tobak, 2016) is defined as temporary water inundation in local depression and over-moistening of arable land due excess water, low runoff, insufficient evaporation and low infiltration capacity of the soil or by upwelling of groundwater (Pásztor, Körösparti, Bozán, Laborczi, & Takács, 2015; van Leeuwen et al., 2016). Based on the direction of the water flow, they are mainly categorized as accumulative inland excess water, upwelling inland excess water and queuing up of inland excess water (Barta, Bata, Benhhe, & Miograd, 2013). The extent and duration of excess water are influenced by the factors related to meteorological, relief-related, geomorphological, hydrological, pedological, groundwater-related, land use and land cover related, as well as human-induced factors (Kuti, Kerék, & Vatai, 2006; Bozán, Körösparti, Pásztor, & Pálfai, 2013; Karoly, et al., 2013; Van Leeuwen et al., 2016).

Although the ponding excess water problem occurs in several low-lying countries, it has received more scientific attention in Hungary (van Leeuwen, 2012). This is due to the fact that more than 45% of Hungary's total area is at risk of PEW inundation (Kuti et al., 2006). On average, 110 000 ha of land is affected annually by PEW in Hungary (van Leeuwen et al., 2016). The major concern is about considerable damage to croplands on low-lying areas (Kozma, 2013; Van Leeuwen et al., 2016). This damage is primarily due to blockage of oxygen and nutrient uptake by ponding condition in the root zone (Barta et al., 2013). Although PEW can have a short-term impact on crop production, frequent and longer duration of PEW can cause long-term damage to the soil in terms of soil texture degradation, salinization, and compaction (Van Leeuwen et al., 2016).

Soil properties are recognized to be one of the main factors influencing the formation of PEW. Soil functions can be limited by prolonged excess water. Frozen topsoil blocks the infiltration, saturated soil limits the infiltration capacity, compacted soil delays the infiltration, and other soil properties such as clay mineral composition, soil texture, organic matter content, storage capacity all can have an impact on the development of PEW (Gál & Farsang, 2013). Soil properties combined with other factors not only affect the formation of PEW but PEW, in turn, physically degrades the soil. In some areas of Hungary, it has caused secondary clay mineral formation in the upper horizon of the soil that has further escalated the risk of PEW formation (Gál, Tóth, Raucsik, Földes, & Farsang, 2017). Subsequently, soil water infiltration response is also affected by soil properties and the soil underneath the ponding.

Soil water infiltration studies are useful in many aspects such as irrigation, runoff generation, soil erosion and nutrient contamination and transport (Kacimov, Al-Ismaily, & Al-Maktoumi, 2010). Poor soil conditions limit the infiltration, redistribution, and storage of water in a soil profile causes more runoff and erosion, and as a consequence reduction of water available to plants (Connolly, 1998). For plant growth, soil with high infiltration rate is generally suitable. Understanding the stability of infiltration data becomes essential to recognize the infiltration capacity of individual soils for better planning against the anticipated hydro-meteorological events (Gundalia, 2018).

It is therefore imperative to accurately quantify the spatial and temporal dynamics of PEW and their relationship to the soil water transport to help farmers or authorities for better adaptation. Optical and microwave sensors are frequently used for mapping PEW inundation. Optical remote sensors (visible, infrared, thermal) are not rarely feasible in persistent cloud cover condition (Bioresita, Puissant, Stumpf, & Malet, 2018) due to their inability to penetrate cloud cover (Huang et al., 2018). On the other hand,

microwave Synthetic Aperture Radar (SAR) has its own source of illumination and can provide information in all weather condtions, day and night, as well as can detect water under vegetation canopies (Brisco, 2015). Furthermore, with multisatellite constellations, it is possible to effectively monitor the spatial and temporal changes of PEW. Additionally, high resolution SAR images combined with high resolution digital terrain model (DTM) can provide information about ponding extent and depth (Giordan et al., 2018). This information derived from satellite data can serve as an input to models and also useful for validation of hydraulic models for quantifying hazard or risk maps. In this regard, this research aims to integrate images with soil water infiltration modelling to identify the extent and areas where PEW occur, when it appears, and how the spaial and temporal extent of ponding can be related to different soil properties.

1.2.   Research problem

This study focuses on Hungary, where two types of water-related hazard are most prominent in the low lying areas; floods and PEW (Barreto et al., 2017). About one-fourth of the population are living in the areas where ponding excess water appears regularly and 60% of the croplands are affected by PEW (Kozma, 2013). Of the many factors, meteorological factors are regarded as the determining dynamic factor where precipitation is the major source for the development of inland excess water (van Leeuwen et al., 2016). Climate change scenarios in Hungary reveals more extreme weather conditions with intensive rainfall events the thus, an increased threat of PEW (Barreto et al., 2017). Due to extreme precipitation, seasonal and permanent excess water inundation has become the most serious agro-environmental issue in Hungary (Pásztor et al., 2015). As a result, adequate information on the spatial and temporal distribution of PEW is crucial for the prevention and management of PEW.

Attempts to assess and monitor PEW in Hungary is carried out in the form of mapping, field measurements, and modelling. These researches are more concentrated towards GIS based hazard or vulnerability mapping via amalgamation of spatial information of factors that affect the formulation of excess water such as soil, agro-geology, relief, groundwater, land cover, rainfall etc. (Pásztor et al., 2006; Bozán et al., 2013; Pásztor et al., 2015). Mapping using optical sensors and radar data has been used to identify the excess water inundations (van Leeuwen, 2012) but mainly at medium resolutions and at a specific date. High-resolution aerial data of 1.5 m was used to map the spatial extent of PEW with the high level of accuracy (Csendes & Mucsi, 2016) but it lacks temporal information. With the advancement of better spatial and temporal resolution of satellite images and free access to the data, Sentinel-1 images combined with multispectral Sentinel-2 and Landsat 8 images were successfully used to identify location and extent of PEW (van Leeuwen, Tobak, Kovács, & Sipos, 2017). All these satellite-based mapping processes in Hungary, however, neglected the temporal analysis of PEW. This study will use a time series of Sentinel-1 images to extract information on ponding characteristics for modelling the dynamics of ponding excess water.

Infiltration is sensitive to soil properties that can directly influence the formation of PEW (van Leeuwen et al., 2016). Knowledge about how fast the water will infiltrate in the soil in case of extreme rain showers and even under excess water inundation condition is important to define soil conservation techniques and planning irrigation and drainage systems. Modelling such responses is limited in Hungary. Modelling of the areas that are affected by PEW are often GIS-based where the risk is estimated based on weighted factors. Researches are dedicated to causes of PEW like soil characteristics, land use, geomorphology, or their interrelation (van Leeuwen et al., 2017). Impact of PEW on soil structure (Gál & Farsang, 2013; Gál et al., 2017) and particle size analysis in ponding location (Gál & Farsang, 2013) has been carried using field and laboratory methods. Inundation mapping from satellite image though provides a good estimate of PEW, it cannot project the status (extent, location, and duration) of inundation to the future. Satellite data integrated with models can provide detailed understanding of PEW development. Therefore, this study aims to develop a soil water infiltration model that can relate information from satellite images to dynamics of ponding excess water formation.

1.3. Research objectives and questions

1.3.1. General Objective

- To describe the dynamics of ponding excess water on agricultural fields based on modelling the infiltration process using data from satellite images and field measurements.

1.3.2. Specific Objectives

1. To assess the difference in soil physical properties in ponding and non-ponding locations.
2. To calibrate a model that describes the process of soil water infiltration in ponding and non-ponding location.
3. To assess the ponding phenomena by linking model output with satellite images

1.3.3. Research Questions

Based on the research objectives, the following research questions are formulated:

Objective 1

- Do the different soil properties explain the variations of infiltration in ponding and non-ponding area?

Objective 2

- What is the infiltration rate of soil underneath selected ponding and non-ponding locations?
- What are the differences in the infiltration processes between the regularly inundated and non-inundated areas?

2. LITERATURE REVEIW

2.1. Ponding excess water mapping in Hungary

Ponding excess water is a threat to many agricultural lands in Hungary. Mapping of ponding excess water in the early days started with labor-intensive field measurements which were then complemented with remote sensing measurements (van Leeuwen, 2012). Many different remote sensing data and techniques were used to map PEW which has increasingly been improved with the recent development of high spatial and temporal resolution images. GIS and remote sensing tools in Hungary have been applied to identify and measure the extent of the PEW in Hungary.

PEW vulnerability mapping PEW has been carried out based on factors such as soil, geology, relief, groundwater, precipitation, land use (Bozán et al., 2009, Pásztor et al., 2006) using a weighted coefficient of each factor. A Complex Inland Excess Water Vulnerability Index (Bozán, et al, 2008; Bozán et al., 2013) map was created based on these factors. Vulnerability maps are also created based on the relative frequency of PEW occurrences that adapted elevation, soil, geological and groundwater (GW) data (Leeuwen & Tobak, 2014). In a more recent research, Artificial Neural Network (ANN) was used that gave better classification results than the traditional methods (van Leeuwen et al., 2017). Simulation results were able to show a clear distinction between water and dry soils. ANN classification provided better results when more GIS datasets were incorporated. These mapping activities has been mostly conducted in North-east and southern part of Hungary.

Leeuwen & Tobak (2014) evaluated the RapidEye imagery (5×5 m resolution) to identify PEW inundations and tested four different methods (unsupervised clustering, maximum likelihood, Spectral mixture analysis, feed forward artificial neural network (ANN) to classify PEW. Due to high temporal resolution, RapidEye imagery was found to be suitable for identification of PEW, but the imagery acquisition needs cost.

van Leeuwen, Tobak, Kovács, & Sipos (2017) developed a workflow that could generate excess water map on a weekly basis using different high resolution satellite data. For this, Sentinel-1 (10×10 m resolution), Sentinel 2 (10×10 m resolution), and multispectral Landsat OLI (30×30 m resolution) images were used and were supplemented with a set of vector files containing information about permanent water and areas where PEW does not occur. All datasets were processed independently and combined to produce an integrated PEW map. A threshold method was used to separate pixels with water and no water for active datasets while for passive datasets unsupervised classification method and Modified Normalized Differential Water Index (MNDWI) was used to classify water classes. These maps were then integrated to produce the one inland excess water map.

To exploit the SAR all-weather, day and night coverage, Yun (2017) used time series of Sentinel-1 images (Oct 2015 to Oct 2016) to map the PEW and its effects on the crop in selected northern and southern sites of Hungary. Mapping of PEW was also supported by Sentinel-2 images, drone images, and field information to verify the existence of ponding water. PEW was identified based on the relationship of time series of rainfall, soil moisture, and NDVI from Sentinel-2 images. Based on the high temporal resolution of Sentinel-1 images, the research was able to identify the occurrence of PEW in the study site. Time series of polarization ratio used to monitor crop growth was found to be strongly correlated with NDVI time series. Based on DEM, the effect of topography on PEW formation was identified in the agricultural fields. Field analysis showed high clay content in the study site but how different properties of soil can have an effect on the formation of PEW was not identified. The recent is the continuation of Yun's work, where this gap will be addressed through field experiments and numerical modelling approach.

2.2.   State of the research on relationship between PEW and with soil properties in Hungary

Gál & Farsang (2013) assessed the impact of PEW on the physical structure of fertile soils *(Chernozems)* in Hungary. The study was carried out in temporarily covered excess water sites analysed from multi-temporal Landsat TM images in the southern part of the Great Hungarian Plain. Soil samples were collected at depths of 0-5, 10-15 and 20-25 cm from inundated areas and non-inundated reference areas. Particle size distribution was measured according to Hungarian standard. Soil compaction detection was measured in terms of penetration resistance and relative soil moisture content. Comparatively higher proportion of clay was measured in inundated area than in non-inundated area characterized by respective silty clayic loam and silty loam texture. High clay proportion was found with increasing depth in both sites with more increase in inundated areas. Volumetric soil moisture was 17% higher in inundated areas. Plough hard pan were identified at depths of 15-20 cm and 40-50 cm from measured penetration resistance that indicated soil compaction.

Barta(2013) analysed the formation of PEW based on hydro-meteorological and soil factors in south-eastern part of Hungary (Tápai-rét area and Batida area). A complex station measuring precipitation, evapotranspiration, soil moisture at three different depths and soil temperature at 5 depths was installed. Defined soil parameters included pH, soil plasticity, carbonate, salt, humus content, bulk density, porosity, field capacity, and hydraulic water conductivity. High clay and low carbonate content with very low permeability were found in the study sites. Soil moisture (SM) and groundwater (GW) at three different depths were compared to analyse the relationship between infiltration and GW excess water. On the Tápai-rét area, PEW of GW origin was analysed. On the other site, accumulative type of excess water was observed especially during autumn and spring precipitation; where soil was almost impermeable, pore volume decreased and due to low evaporation and low infiltration, the soil retained water at the surface. Infiltration capacity increased during the summer periods when there was high ET. Moisture content was found as the most influencing factor of infiltration rate among other affecting factors. The findings suggested that through continuous monitoring of SM in several depth, it is possible to predict PEW.

Gál et al. (2017) used X-ray computer tomography (XRCT) and X-ray powder diffraction (XRPD) method to detect effects of PEW on bulk density and clay mineralogy. Intact soil core samples were taken in PVC cylinders of 28-32cm height and 19 cm diameter from an inundated and non-inundated location in Békés County, in the Southern Hungarian Great Plain. Results showed higher bulk density and compaction recorded by XRCT from inundated locations. Likewise, a higher proportion of secondary clay mineral formation was observed in the upper horizon of the inundated samples compared to the non-inundated locations. All these researches have analysed properties of soil in inundated areas but the infiltration response in the affected areas was not modelled.

3. STUDY AREA AND DATASET

3.1. Description of the study site

3.1.1. Location

The research was carried out in Hungary (47° 29' 52" N, 19° 2' 24" E), where the majority of the land is used for cultivation (58.7 %). Hungary is a country with 68% of the area below 200 m altitude, 30 % is covered by hills (200 to 400m), and only 2 % above 400 m (Barreto et al., 2017). The highest elevation of Hungary is 1014 m. The study site was located in northern agricultural land of Heves county, which is about 108 km from the capital city, Budapest. Two selected plots with experimental points is shown in Figure 1. The area is characterized by incessant PEW nuisance, which occurs in the local depressions. The PEW problem has also been mapped in the area using time series of Sentinel images by Yun (2017).
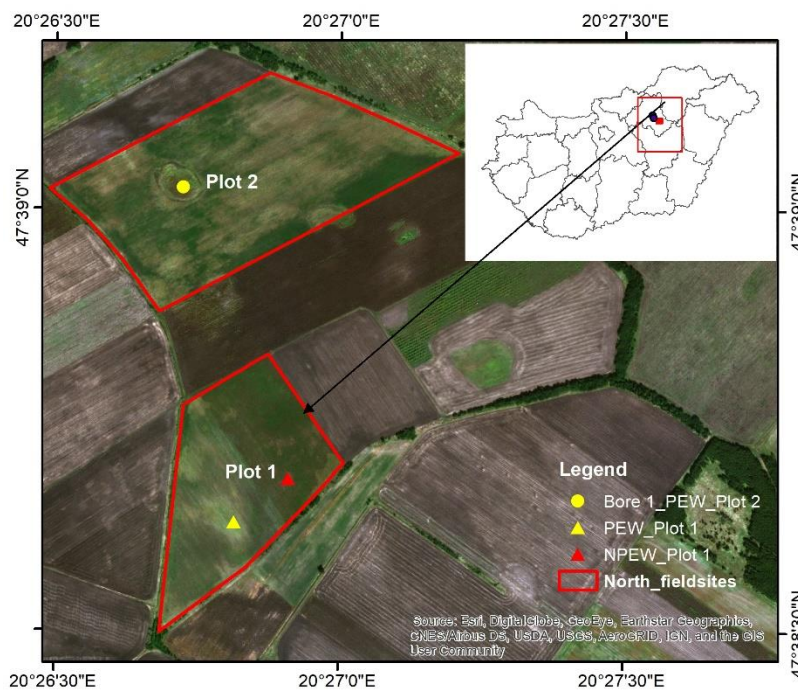
Figure 1: Study area showing sample location of ponding excess water (PEW in yellow) and non-ponding excess water (NPEW in red)

3.1.2. Climate

The climate of Hungary is continental, with Atlantic and Mediterranean influences. The average temperature is 8 to 11°C, where January is the coldest and July is the hottest month. Annual precipitation ranges from 500 to 900 mm, where the Great Plain receives the lowest amount while western Hungary gets the highest amount (Barreto et al., 2017). Wet periods are observed between May to June and in the autumn (October to November). Potential evaporation is high during the summer wet period but it is less during November to March (Yun, 2017). High events of rainfall combined with low potential evaporation during this period often cause ponding problems in Hungary. Annual snow coverage is 41days/year (Faragó, Láng, & Csete, 2010). Hungary is rich in groundwater with an average depth of shallow groundwater of 2-5 m (Barreto et al., 2017).
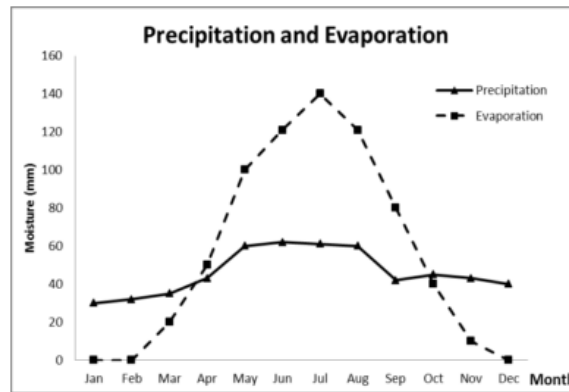
Figure 2: Monthly mean precipitation and evaporation of Hungary (Yun, 2017).

3.1.3. Soils of Hungary

The soils of Hungary are grouped according to soil forming factors and process (Mezősi, 2017). The major soil types of Hungary are grouped into nine categories based on climatic, geographical, and genetic bases as shown in Figure 3. In mountainous areas, fertile Luvisols are found that are developed under high precipitation and low temperature conditions. Such soils are characterized by accumulation of clay in the subsoil. In lowland areas, dark fertile Chernozems are found, which the most fertile soil of Hungary is. In between mountains and Hungarian Plain, young brown soil known as Cambisols are found. Fluvisols are also found in river valleys or floodplain areas that shows layering of the sediments. Soil deposited on windblown sands known as Arenosols are also found in certain areas of Hungary. Salt affected soils known as Solonchaks and Solonetzs are also found in areas where groundwater containing soluble salts are found close to the surface. Based on field observation, the soil type in the study site is characterized by swelling clays (Annex 2) with and seasonal cracking of soil, which is the characteristics of Vertisols.
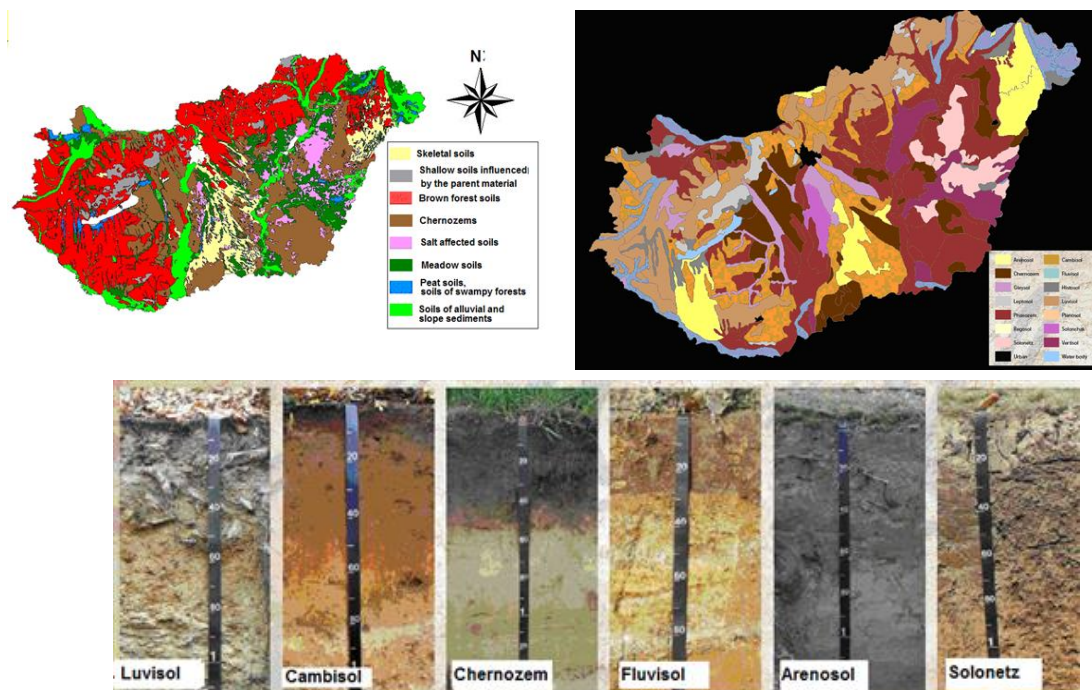
3.1.4. Land cover and land use

Land cover in the Heves County (3600.32 km²) is primarily cropland (52.3%), forest (22.08%) and grassland (11%). Alfalfa, rapeseed, and wheat are the main crops grown in the region. In the experimental site, alfalfa was mainly grown in the study period, which was under growing stage with crop height of 10cm (Yun, 2017). The experimental plots are protected under the Natura2000 program of Europe. Figure 4 shows the land cover of the study area located in Heves County.
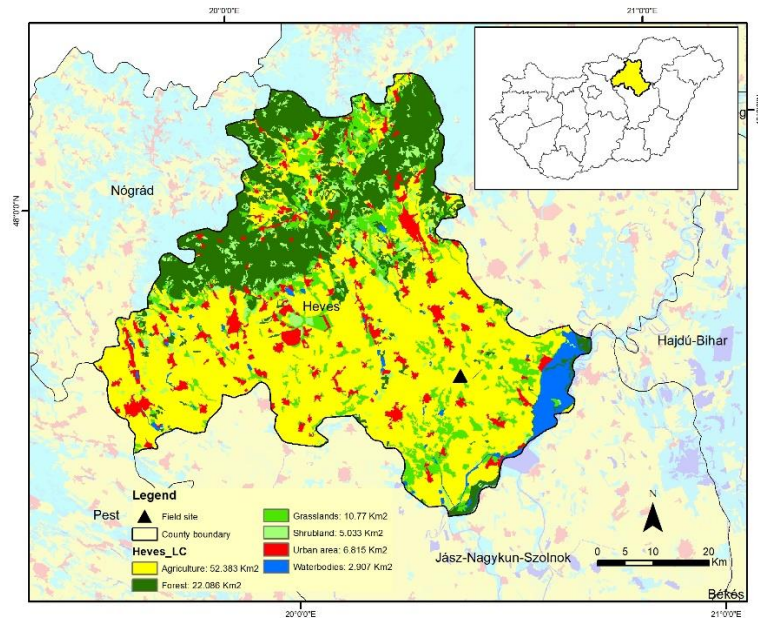
Figure 4: Landcover map of Heves County based on 100m Corine Landcover of 2018

3.2.   Datasets:

3.2.1. Soil Properties

Soil physical datasets such as soil texture, grain size, bulk density, porosity, soil water content, organic carbon, satuarted hydraulic conductivity were measured in the laboratory. These measured parameters were further used to estimate soil hydraulic paramters of van Genuchten (VG) model using different pedotransfer functions (PTF). The laboratory measurements were also compared with the global 250m soil grids dataset.

3.2.2. Satellite data

Satellite data in this study entailed acquisition of processed Level-1 Ground Range Detected (GRD) Sentinel-1A C-band (5.405GHz) images from September 2015 to September 2016 from past work conducted by (Yun, 2017) Yun (2017). An Interferometeric Wide swath (IW) swath mode with 250 km swath, 5x20 m spatial resolution and a temporal resolution of 5 to 7 days and burst synchronization for interferometry was used for mapping of PEW in Northern part of Hungary. The images used in the analysis were form the ascending orbit.

---

[1] https://www.tankonyvtar.hu/en/tartalom/tamop425/0032_talajtan/ch12.html

3.2.3. Meteorological data

The meteorological data required were daily values of precipitation, maximum and minimum temperature, relative humidity, wind speed, and sunshine hours. Due to difficulty in accessing the in situ data, different sources were used to collect data as shown in Table 1 Precipitation and maximum and minimum air temperature data of Bogács station (located at 20.28 km N of the study site at 47.90° latitude and 20.53° longitude and elevation of about 170 m) (Sept 2018 to Dec 2018) and Mezőkövesd station (located at 29.65 km north of study site at 47.80° latitude and 20.57° longitude and elevation of about 114m) (2015 to 2016) was collected from website Metnet[2] for the periods of 2018 and 2015 to 2016 respectively. Similarly, relative humidity and wind speed data was collected from station Füzesabony (located at 47.75 °N, 20.41 °E and elevation of about 112m) from the Wunderground[3] website. Furthermore, daily sunshine hour's data was extracted from ERA-Interim, which has a resolution of 80 km. Figure 5 shows the monthly distribution of precipitation (Bogács and Mezőkövesd stations) and the average temperature recorded at Bogács station and other variables recorded at station Füzesabony. High rainfall accumulation in the January and February and with very low temperature recorded during this month form suitable conditions for the excess water formation on the surface.
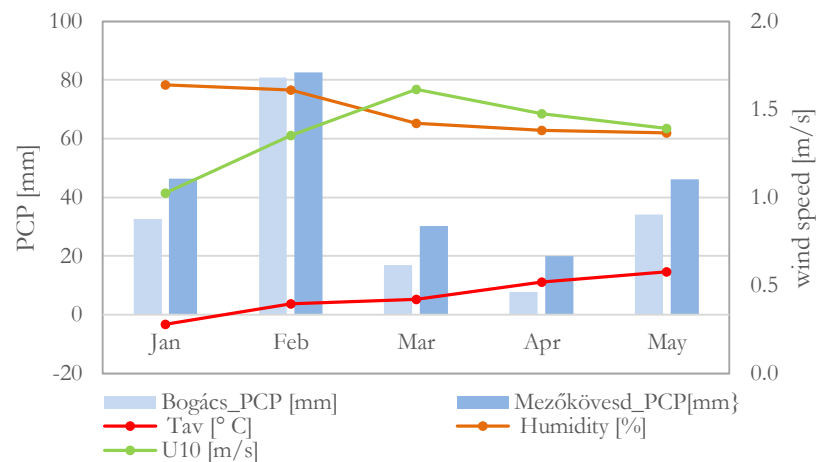
Figure 5: Monthly distribution of meteorological variables in 2016

3.2.4. Digital elevation data

Digital elevation model (DEM) from previous work by Yun (2017) was used. DEM was created from aerial photos taken by a DJI Phantom4 drone at a relative flying of 90 m. A 3.5 cm DEM created with vertical accuracy of 3 to 4 cm was used to calculate the time series of water depth in the inundated area. Inundation in plot 1 was noted to occur in lower depression about 87.9 m in the Northern site 1 (Figure)
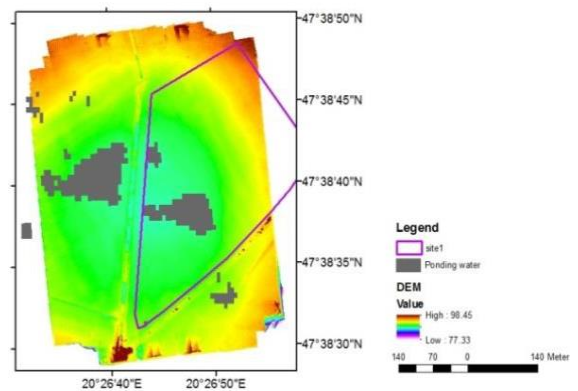
Figure 6: DEM of North site 1

---

[2] https://www.metnet.hu/

[3] https://www.wunderground.com/history/daily/hu/f%C3%BCzesabony/IHEVESCO3/date/2018-1-8

Table 1: Summary of datasets used in the study

Data	Type	Data period	Source
Sentinel images	1A	Oct 2015 to Oct 2016	Copernicus hub[4]
Soil data	Soil physical parameters		Field and laboratory data
	Soil moisture and temperature	Sep 25, 2018 to Dec 5, 2018	Soil sensors
	Raster soil data		Soil Grids[5]
Meteorological data	Precipitation, Air temperature	Sep to Dec, 2018 & Sept 2015 to Mar 2016	Station:Bogács; Metnet
	Relative Humidity, Wind speed		Station:Fuzesobony; Wunder ground
	Sunshine hours		ECMWF[6]
DEM	Drone image		Yun (2017)
Crop data	Farmer's log		

[4] https://scihub.copernicus.eu/dhus/#/home
[5] https://soilgrids.org/#!/?layer=ORCDRC_M_sl2_250m&vector=1
[6] https://www.ecmwf.int/en/forecasts/datasets/archive-datasets/reanalysis-datasets/era-interim

4. MATERIALS AND METHODS

4.1. Research structure
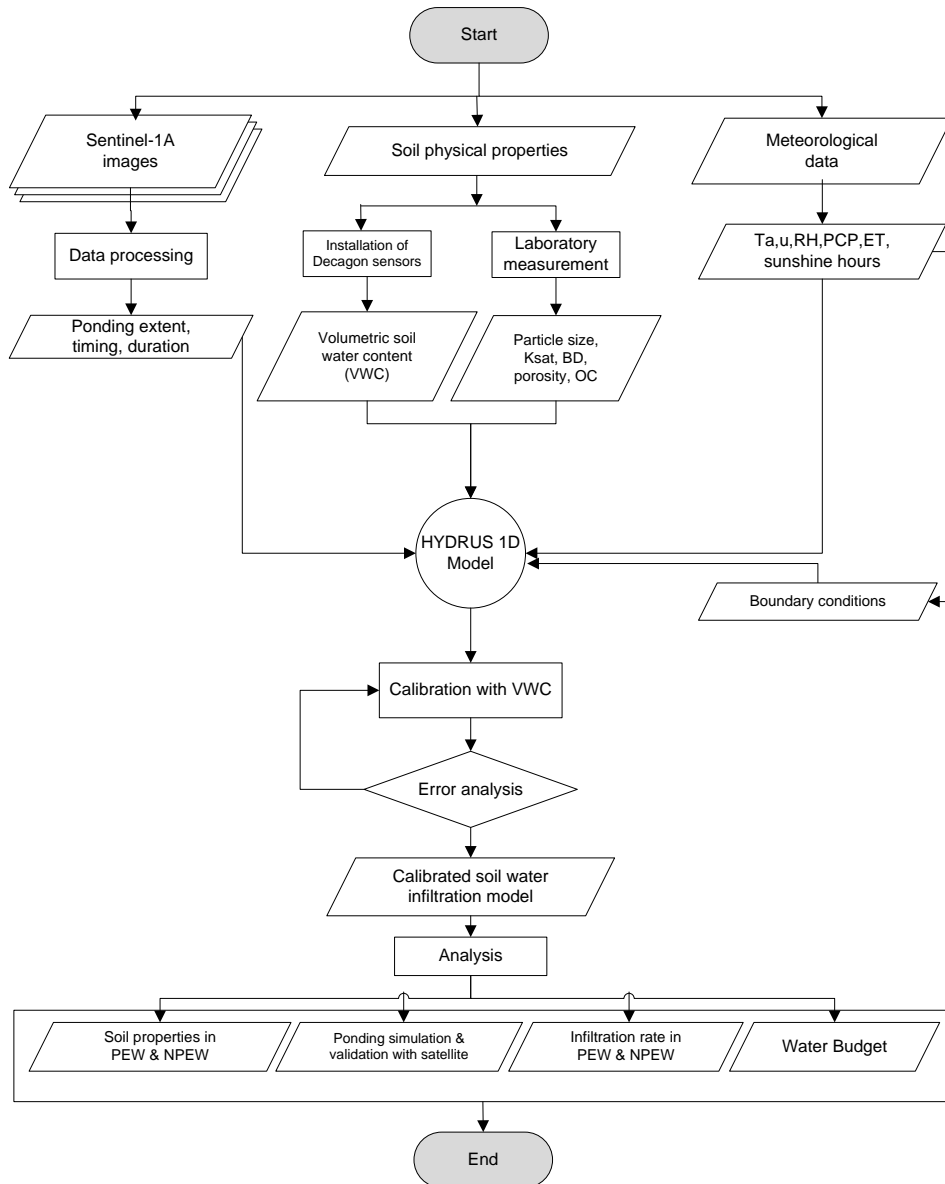
Figure 7: Flowchart showing the methodological approach of the study

Figure 7 provides the overview of the research approach followed in this study. To meet the objectives of this study, site specific soil physical parameters, meteorological data, and satellite data were integrated to model the infiltration process. Field and laboratory measurements were carried out to collect information related to soil. A one-dimensional HYDRUS model was established based on field measured soil water content in different locations. This established model was used to simulate the ponding, which was validated with satellite derived information. The soil water infiltration process under such conditions were further analysed. The section below briefly elaborates the approaches and findings of this study.

4.2. Field data collection

4.2.1. Soil sample collection

To determine the soil physical properties (SPP) in the PEW and NPEW sites, fieldwork was conducted from 16th September to 2nd October 2018. Before selection of the test site, a reconnaissance survey was carried out in several plots of Northern farmland. Plots with regular ponding areas were then identified based on consultation with the local farmers, depression observed in the area, type of vegetation grown in the area and past inundation mapping carried out in the region. As shown in Figure 1, Plot 1 and Plot 2 were selected for the field experiment. Two pits were dug in plot 1 i.e. PEW problem area and other in NPEW area, while soil samples were also collected from boreholes using core-sampler from plot 2 which is also prone to PEW formation. However, comparative analysis of SPP in inundation and non-inundation sites was only carried out from samples collected from plot 1. Basic description of the field site is shown in the table below:

Table 2: Site description

	Plot 1_NPEW	Plot 1_PEW	Plot 2_Bore1
Date	23/9/2018	25/9/2018	26/9/2018
Lat.	47 38 40.8 N	47 38 37.7 N	47 39 01.5 N
Long.	20 26 54.7 E	20 26 49.0 E	20 26 43.5 E
Land use	• Alfalfa field, covered with sparse vegetation of about 10 cm in length • Root length observed at 30-40 cm. • Maximum rooting depth was observed around 80cm • Area protected under Natura 2000	• Covered with dry grass of about 10 cm in length • Root length observed at about 30-40 cm • Area protected under Natura 2000	• Covered with dry grass about 40 cm length and surrounded by alfalfa field
Soil profile	• Samples collected down to a depth of 250 cm • Top 30 to 40 cm drier, angular soil aggregates with roots • 40 to 60 cm with mixture of black and faint yellow soil • 60 to 120 increasing yellow soil with depth • Moisture increasing with depth	• Samples collected down to a depth of 310 cm • Top 30 to 40 cm drier, angular soil aggregates with roots • 40 to 100 cm with heavy uniform black strongly bounded soil • Moisture increasing with depth	• Samples collected down to a depth of 180 cm • Top 30 cm drier • 40 to 150 cm with heavy black strongly bounded soil • Moisture increasing with depth
Field site			

Soil samples were collected from 150 cm deep pits in plot 1, where both undisturbed and disturbed soil samples were collected. An excavator was used for digging pits in plot 1, while soil auger was used to collect samples from deeper depths in plot 1 and also in plot 2. Bore logs was created for deeper profile in both

sites (Figure 8). Initially, a total of 68 soil samples (24 undisturbed and 44 disturbed) were collected at a depth of 10 cm interval from four different sites. But due to time limitation, the samples were prioritized and reduced to the laboratory analysis of 33 samples in total.

In plot 1, 11 undisturbed soil sample (UDSS) and 4 disturbed soil samples (DSS) were collected and analysed at different depths from the PEW site. Similarly, 10 UDSS and 4 DSS were collected and analysed from NPEW site. While from plot 2, only 4 DSS were collected and analysed from ponding location to see the resemblance of soil properties in ponding areas. The model was, thus, only developed in plot 1 for two areas. The collection of the sample at different depths was based on heterogeneity such as colour and texture observed in the soil profile in both pits. UDSS were collected using steel core sampler of 5 cm in diameter and 5.1 cm in height (100.1 cm³ volume). The core rings were completely inserted in the selected depth of the walls of the pit (perpendicular to the pit wall) with the help of hammer to ensure the soils were undisturbed. Steel core sampler was then carefully removed by scraping soils around the sampler with a knife. Samples taken out were levelled to the ring height with the help of knife and labelled caps were enclosed to the rings. DSS was collected in plastic soil sample bags using knife from the selected depths of the walls of the pit. UDSS were used for measuring saturated hydraulic conductivity (K_{sat}), bulk density (BD), porosity, organic carbon, water content and particle size. Likewise, DSS was mainly used for particle size analysis and organic carbon. Cosby, et al. (1984) and Hillel (2003)equations were used to determine porosity and BD respectively from DSS.

Figure 8 : Pits installed with soil moisture sensors in NPEW (a) and PEW (c) in plot 1; Bore logs of deeper profiles in NPEW (>120 to 250 cm) (b), PEW (>150 to 310 cm) (d) in plot 1 and PEW (e) in plot 2 (0-180 cm).

4.2.2.   Volumetric water content (VWC) measurement

In both pits, Decagon 5TM/5TE soil moisture sensors were installed to measure VWC. Each site was installed with 5 sensors vertically at the wall of the pit at various depths of 5, 15, 40, 90, 150 cm at the PEW and 5, 15, 40, 80, 12 cm at the NPEW locations. Internal calibration function for minerals soils with a measurement accuracy of 4% VWC was used. The measurement interval was set to 15 minutes. The probes were connected to EM50 Decagon data loggers that were sealed by plastic bags and buried in the soil for protection. Data was downloaded from loggers via USB cable using DataTrac 3 software. The measured VWC was used for initialization and calibration of the model. Figure 9 shows the volumetric soil moisture measurement from sensors at various depth for two sites.
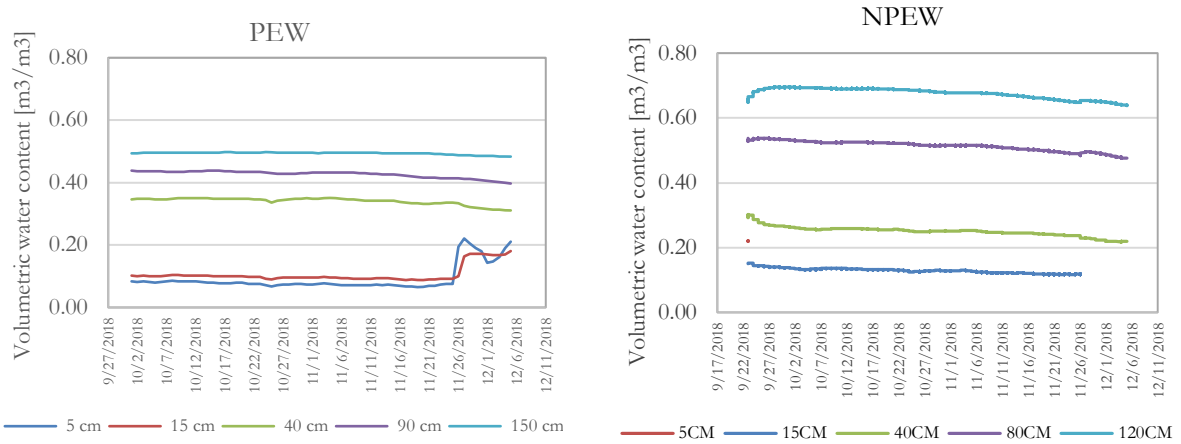
Figure 9 : Volumetric water content (VWC) measurement with respect to depth in ponding and NPEW location

4.3. Laboratory measurement of soil physical property

4.3.1. Soil particle size distribution

Disturbed and undisturbed soil samples collected from several depths in the field were processed in the geoscience laboratory of ITC to determine the fraction of sand, silt and clay content in the soil. Grain size was analysed based on ISRIC protocol (van Reeuwijk, 2002) using the pipette method. Soil textural classes were categorised based on the USDA system.

The pipette method first entailed oxidation of organic matter in soil samples by using Hydrogenperoxide (H_2O_2), then using a dispersing agent - sodium hexameta phosphate ($NaPO3)6$ to disperse the soil sample in the water and finally prepare a suspension for subsequent determination of particle size groups by sedimentation techniques. The sand fraction was separated from silt and clay by 50μm sieve. Silt (20-50 μm) and clay fraction (<2 μm) were measured using sedimentation technique whereby samples were pipetted as a function of room temperature and settling time. The room temperature during the experiment was 21°C, and silt and clay fractions were measured at a depth of 13.8 cm and 7 cm respectively.

4.3.2. Saturated hydraulic conductivity (Ksat)

The laboratory permeameter from Eijkelkamp (Eijkelkamp Soil and Water, 2017) was used for measuring saturated hydraulic conductivity. For all the samples collected, Ksat was measured using the constant head method. Depending on the nature of soils, samples collected in the ring were left to saturate in water tank either overnight or for several weeks. The saturated rings were placed in a ring holder and then put in the container of the permeameter, where a continuous supply of water was maintained at a certain level with the help of a regulator. Due to differences in pressure inside and outside of the ring holder, saturated water in the soil rings are pushed upward in the ring holder. A plastic siphon filled with water was then placed partly inside and outside of the ring holder, which created a difference in water level inside and outside of the ring holder. This differences in head ensured the continuous flow of water that is passed through a measuring burette. Water flowing through the burette was measured at a fixed time periods until the rate of flow of water became constant. The measured head differences and the rate of flow was used to determine K_{sat} using Darcy's equation (Eqn. 1)

$$K_{sat} = (V \times L)/(A \times t \times h)$$ *Eqn. 1*

Where,

K_{sat} is saturated hydraulic conductivity (cm/d), V is volume measured in burette (1 cm³), A is the cross-section of the sample (cm²), t is the length of time lapse (day), L is the length of soil sample (cm), ΔH is the water level difference between inside and outside of the ring holder (cm).

4.3.3. Estimation of soil physical parameters (Bulk density, Porosity, SWC, organic carbon)

Bulk density (BD) is defined as the mass of a unit volume of dry soil (Eqn. 2). Soil samples in the soil rings were dried in oven at 105°C for 24 hours and weights were measured. Subsequently, soil porosity (∅) was calculated based on measured bulk density using Eqn. 3 (Hillel, 2003). Soil organic carbon was also measured in the laboratory using PerkinElmer 2400 Series II CHNS/O elemental analyzer[7] system. The initial soil water content (SWC_d) and saturated soil water content of the collected samples in the soil rings were also measured on dry and wet basis in the laboratory. For the UDSS, porosity and BD is estimated based on Cosby et *al.* (1984) and Hillel (2003) Eqn. 3 and 4 respectively.

$$Bulk\ density\ (\tfrac{g}{cm3})\ = \tfrac{W_d}{V} \qquad\qquad \textit{Eqn. 2}$$

$$\emptyset\ (\% = 0.489 - 0.001268 \times (\%sand) \qquad \textit{Eqn. 3}$$

$$\emptyset\ (\%) = 1 - \tfrac{\rho_b}{\rho_s} \times 100 \qquad\qquad \textit{Eqn. 4}$$

$$SWC_d\ (\%) = \tfrac{W_i - W_d}{W_d} \qquad\qquad \textit{Eqn. 5}$$

Where, W_d is the oven dry weight (105°C) of soil, V is the volume of soil ring (100.138 cm³ i.e. 5cm diameter*5.1cm height), ρ_b is the bulk density (g cm⁻³), ρ_s is the mineral particle density of about 2.65 (g cm⁻³), W_i is the initial weight of the soil sample in the soil ring.

4.4. Satellite data

Pre-processing of Sentinel-1 data included radiometric calibration, geometric correction of SAR images, view angle correction and speckle filtering of SAR images. Methods such as Range-Doppler Terrain Correction, normalizing the incidence angle with a reference angle (average view angle 38.9°) and refined Lee filter for speckle filtering was used (Yun, 2017). VV polarized backscatter was used to detect ponding. Several homogenous polygons as a mask were used for calculating mean backscatter coefficient. Pixels with low backscatter value was then set as a threshold to differentiate PEW and NPEW region. Pixel with values greater than the threshold was identified as non-ponding areas while with low value as ponding areas.

Several sites were used to map PEW by Yun, (2017). Site1 was selected in this study, which is a plot of 0.114 km². The backscatter value of -18dB was observed to remain constant from January to March, indicating ponding in the area (Figure 10). Fourteen images were used during the period for time series analysis (Figure 11). Ponding was not detected in 1/4/2016, 1/28/2016 and 3/11/2016 out of fourteen images. Ponding was found to occur during winter that appeared from 1/11/2016 to 3/28/2016 with different extent as shown in figure 11. This information of timing of ponding and duration, mapped from the images were used for modelling PEW using HYDRUS.

---

[7] http://www.perkinelmer.com/product/2400-chns-o-series-ii-system-100v-n2410650
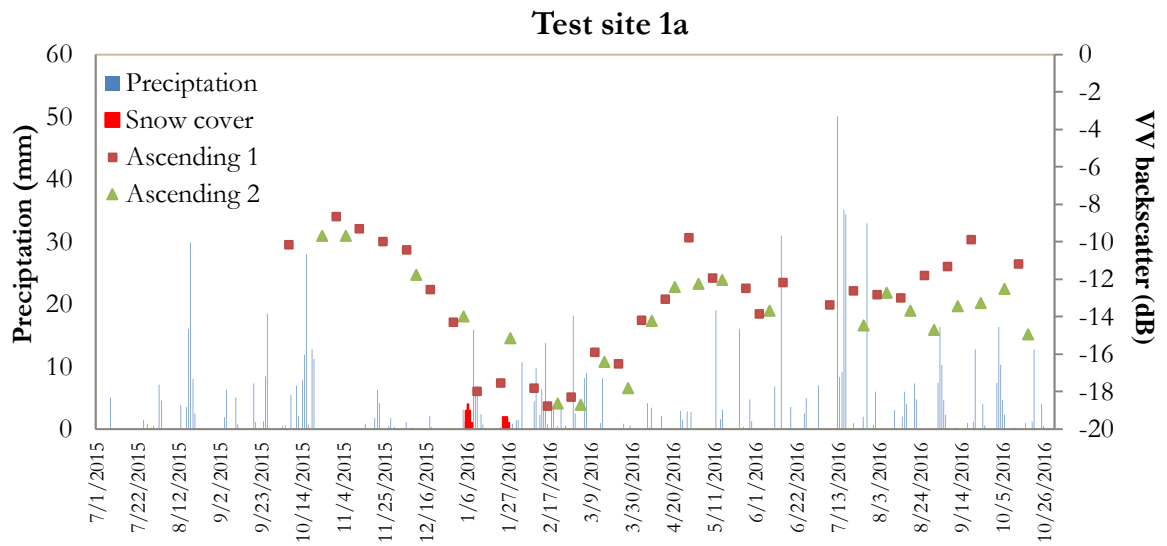
Figure 10: Low backscatter values used for the identification of ponding period (Yun, 2017)
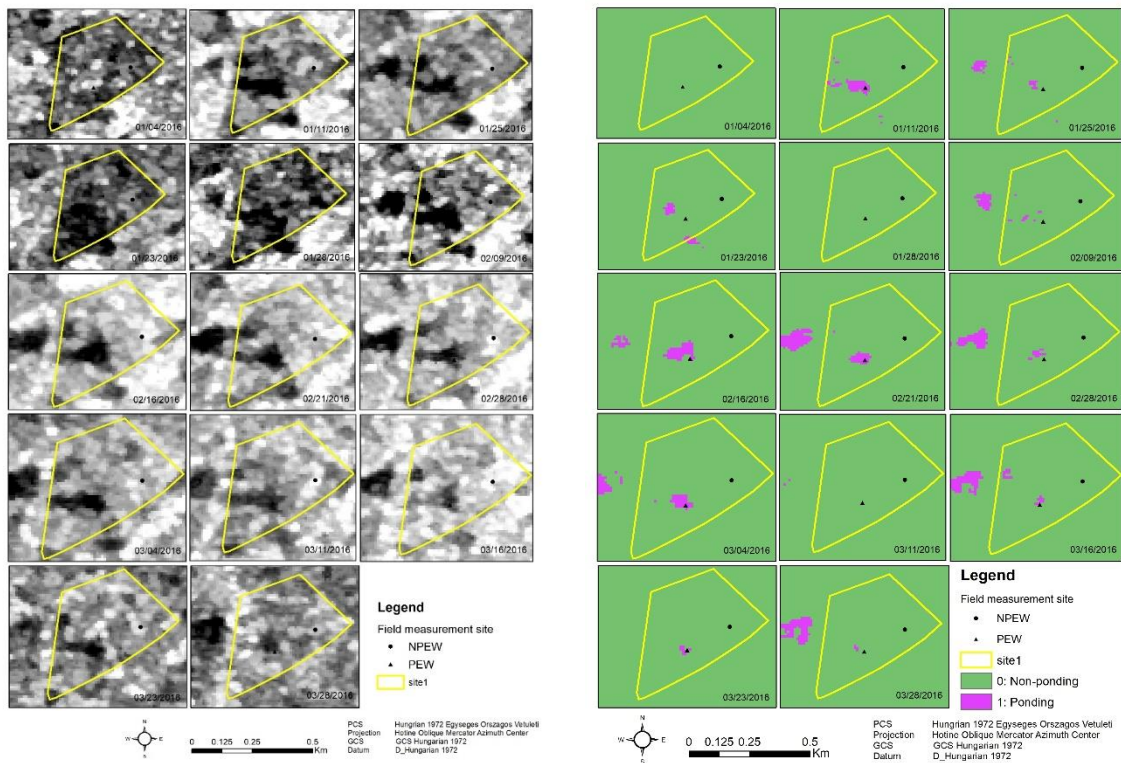
Figure 11: Time series of processed Sentinel 1A images (left) and binary map (right) of PEW in plot 1 prepared based on dataset by Yun (2017).

4.5. Numerical Model

4.5.1. HYDRUS -1D model set up

Numerical simulations in a multi-layered heterogeneous soil profile was carried out using HYDRUS-1D (version 4.16.0110). HYDRUS is a program for simulating water, heat and solute transport in both saturated and unsaturated media (Šimůnek e al., 2013). One dimensional water movement was simulated in this study. For this, inputs included meteorological data and soil properties. Precipitation and evapotranspiration were the main forcing components in the model. Data related to the medium included soil texture, water retention curve parameters, hydraulic conductivity, and root distribution parameters. The soil hydraulic parameters (SHP) were estimated from grain size distribution data using different pedo-transfer functions (PTF), and were used to calibrate the model against the soil water content measurements at different depths. The measured profile was then used to assess the performance of the built model. This calibrated model was then applied to study the ponding dynamics and infiltration behavior under such conditions.

Water flow in HYDRUS 1D is governed by a modified form of the 1D Richards equation (Eqn. 6), which is derived by considering conservation of mass and Darcy's law of water flow through a porous medium. This governing flow and transport equation is solved numerically using Galerkin-type linear finite element schemes (Šimůnek e al., 2013).

$$\frac{\partial \theta}{\partial t} = \frac{\partial}{\partial z}\left[K(h)\frac{\partial h}{\partial z} + 1\right] - S(z,t) \qquad \text{\textit{Eqn. 6}}$$

Where, $\partial\theta/\partial t$ is the change in volumetric water content (cm^3 cm^{-3}) per unit time (t), h is the soil water pressure head (cm), $h>0$ means saturated condition and $h<0$ means under unsaturated condition, z is vertical space coordinate (cm), K is the hydraulic conductivity coefficient (cm day^{-1}), and S is the root water uptake rate (cm day^{-1}).

4.5.2. Geometry and iteration criteria

A one-dimensional soil profile of 310 and 250 cm in depth was considered in PEW and NPEW respectively. The soil profile was established based on the results on soil texture analysis in the laboratory (Figure 12). Soil hydraulic parameters were assigned on the basis of materials distributed in the profile. Generally, the smaller spacing is assigned close to the soil surface where large hydraulic gradients occur (Šimůnek, et al. 2012). Considering the computations to be carried out in the heterogeneous soil profile layer, where sharp gradients could occur at the interface of the contrasting layers (Šimůnek, et al. 2012), the soil column in each site was discretized by a uniform and closer spacing of 1cm (i.e. 310 nodes in PEW and 250 nodes in NPEW).

The maximum number of iterations, water content tolerance and pressure head tolerance were defined 40, 0.1 and 1 cm, respectively, to limit the mass balance errors between time steps. Changes in water contents were calculated by the model at successive nodes until a selected level of solution convergence was reached. Five observation nodes were placed at the same depth where soil moisture sensors were placed in the field i.e. at 5, 15, 40, 90, and 150 cm in the PEW location and at 5, 15, 40, 80, and 120 cm in NPEW location. The output solutions of water content were compared at the observation nodes.
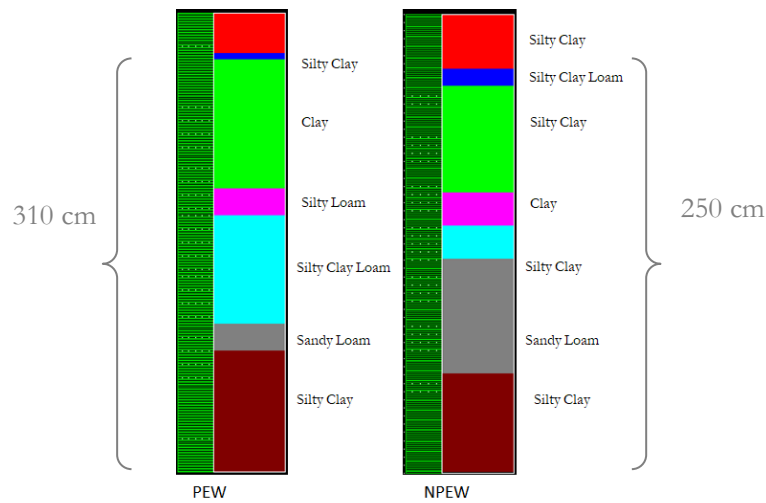
Figure 12: Spatial discretization of soil profiles according to soil textural classifications

4.5.3. Initialization and boundary conditions

Initialization is an important aspect in solving the Richards equations across the model domain. Initial values in this study were defined in terms of water content (θ). Soil water contents measured from Decagon sensors at specified depths on first considered day of the measurement were given as initial conditions to the model at a daily time step. Values between the observation nodes were linearly interpolated from the measured values. Table 3 shows the initial soil moisture data at the observation nodes.

Table 3: Initial soil moisture values [cm^3 cm^{-3}] defined in the model

Location/Depth	5 cm	15 cm	40 cm	80 cm	90 cm	120 cm	150 cm
PEW	0.09	0.11	0.34		0.43		0.49
NPEW	0.22	0.13	0.25	0.51		0.68	

The soil profile was subjected to two boundary conditions at the surface and bottom of the profile defined. At the surface, a time variable system dependent boundary condition was applied meaning that the boundary condition depends on the solution at the end of each time step (Šimůnek e *al.*, 2013). Soil water movement through upper boundary in this study mainly involved evaporation and infiltration in a vertical direction. The horizontal movement of water transport was ignored. Therefore, no flow boundary conditions were applied to the left and right side of the study area.

In the PEW location, the surface was exposed to the atmospheric boundary condition, where inflow to the profile was considered in the form of precipitation (as negative) to soil profile whereas outflow in the form of evapotranspiration (positive) was considered. The upper boundary condition allowed water to build up in the cases of increased precipitation and reduced infiltration and evapotranspiration. During fieldwork, the groundwater level at the PEW location was identified at a shallow depth of 310cm. But due to lack of time series of water level data, a constant flux of zero was specified at the bottom of the profile.

In case of the NPEW location, atmospheric boundary condition with surface runoff was applied at the surface and with unknown groundwater depth, free drainage was applied as the bottom boundary. The hysteresis effect was ignored in this study due to the lack of data.

4.5.4. Soil Hydraulic Parameters

Soil hydraulic parameters are the critical input parameters for simulating water availability and transport in soils (Emilio et al., 2018). High spatial variability of these properties makes it difficult for direct measurement either in field or in laboratory. Therefore, numerous pedotransfer functions have been developed that uses regression equations to predict the difficult to obtain parameters from more easily measured soil properties(Perfect, 2003). PTFs are widely used approach to indirectly estimate the hydraulic properties based on available soil characteristics such as particle size distribution, bulk density, porosity, organic matter (Pachepsky and Rawls, 2004). The soil water movement in this study is described by soil hydraulic functions defined by Van Genuchten (1980) and Maulem (1976), which is the most widely used equation.

$$\theta(h) = \begin{cases} \theta_r + \frac{\theta_s - \theta_r}{[1+|\propto h|^n]^m}, & h < 0 \\ \theta_s, & h \geq 0 \end{cases} \qquad \textit{Eqn. 7}$$

$$K(h) = \begin{cases} K_s S_e^l [1 - S_e^{1/m}]^2, & h < 0 \\ K_{sat}, & h \geq 0 \end{cases} \qquad \textit{Eqn. 8}$$

$$S_e = (\theta - \theta_r)/(\theta_s - \theta_r) \qquad \textit{Eqn. 9}$$

$$m = 1 - \frac{1}{n}, n > 1 \qquad \textit{Eqn. 10}$$

Where, θ_s and θ_r are the saturated and residual water contents (cm³ cm⁻³) respectively, l is the tortuosity parameter, $Ksat$ is the saturated hydraulic conductivity (cm day⁻¹), Se is the effective saturation, and $a, m,$ and n are the empirically fitted parameters.

Van Genuchten (VG) hydraulic parameters are predicted by numerous PTFs. HYDRUS uses the Rosetta PTF software package, developed by (Schaap et al., 2001) to predict van Genuchten parameters using Maulem's pore size model. Rosetta uses a neural network method to estimate SHP based on data from 2132 water retention samples and 1306 saturated hydraulic conductivity (K_{sat}) samples of North America and Europe (Schaap et al., 2001). Prediction from Rosetta is possible through soil textural class information, particle size data (PSD) PSD combined with bulk density (BD) and water retention points as input. Rosetta model was used within HYDRUS to estimate the soil hydraulic parameters for this research using the first three approaches. However, PSD combined with BD was used as the first attempt for the calibration.

Besides the Rosetta model, several other PTFs used to estimate VG parameters (Table 5) were used to define the range of uncertainty in water retention parameters. The selected PTFs expresses the magnitude by utilizing the PSD such as sand, silty, clay, bulk density and organic matter (OM) (Table 4). Perchepsky et al. (1982) applied VG model in Hungarian national database using the fraction of sand, clay and BD data. Wosten et al., (1999) analyzed all Europe database and derived PTF based on the database of Hydraulic Properties of European Soils (HYPRES) to estimate VG parameters. Since the field site contained high clay content, multiple PTFs incorporating clay content and other measured parameters (Table 1) were mostly opted other than soil texture only.

Table 4: List of PTFs for estimate to estimate soil water retention curve

PTF's	Sand%	Silt%	Clay%	OM %	BD
Pachepsky et al. (1982)	√		√		√
Rawls et al. (1982)	√	√	√		√
Rawls & Brakensiek (1989)	√		√		√
Rosetta (Schaap et al., 2001)	√	√	√		√
Vereecken & Feyen (1989)	√		√	√	√
Wosten et al., (1999)	√	√	√		
Wösten et al. (2001)	√	√	√	√	√
Weynants et al. (2009)	√			√	√

Table 5: Estimated range of parameters based on PTFs used as in Table 4

Depth	Soil texture	θr [cm³ cm⁻³]	θs [cm³ cm⁻³]	α [cm⁻¹]	n	Ksat [cm day⁻¹]
0-5 cm	Silty clay	0-0.32	0.36-0.52	0.005-0.0186	0.408-1321	0.15-31.20
5-100 cm	Clay	0-0.31	0.38-0.52	0.008-0.0204	0.444-1.296	0.02-33.96
100-120 cm	Silty loam	0-0.11	0.39-0.46	0.0053-0.0162	0.401-1.663	1.39-59.59
120-190 cm	Silty clay loam	0-0.23	0.37-0.48	0.0051-3.972	0.396-1.520	0.55-17.99
190-220	Sandy loam	0-0.09	0.32-0.41	0.0262-8.626	0.363-1.890	3.96-317.99
220 to 310 cm	Silty clay	0-0.51	0.36-0.52	0.005-0.0355	0.404-1.361	0.28-61.94
NPEW						
0-15	Silty clay	0-0.27	0.36-0.48	0.005-0.093	0.41-1.41	0.48-34.91
15-40 cm	Silty clay Loam	0-0.24	0.03-0.49	0.008-0.193	0.43-1.52	0.48-37.73
40-80 cm	Silty clay	0-0.32	0.36-0.51	0.005-0.017	0.43-1.32	0.05-29.09
80-100 cm	Clay	0-0.36	0.380-0.77	0.005-0.018	0.41-1.28	0.06-29.93
100-120 cm	Silty clay	0-0.44	0.36-0.52	0.001-0.019	0.42-1.32	0.01-18.64
120-190 cm	Sandy loam	0-0.10	0.37-0.51	0.018-14.320	0.37-1.89	4.60-106.10
190-250 cm	Silty clay	0-0.28	0.36-0.50	0.005-0.035	0.41-1.35	0.28-53.15

4.5.5. Evapotranspiration

The potential evapotranspiration was computed according to Penman-Monteith equation that combines the meteorological information with radiation component, as recommended by FAO (Allen et *al.,* 1998). Daily time series of meteorological data such as minimum and maximum temperature (°C), relative humidity (%), wind speed (km/day), sunshine hours was collected from different sources as shown in Table 1 for computing ET_0 (Eqn. 11).

$$ET_0 = \frac{0.408\Delta(R_n-G)+\gamma\frac{900}{T_{mean}}u_2(e_s-e_a)}{\Delta+\gamma(1+0.34u^2)} \qquad \textit{Eqn. 11}$$

Where ET_0 is reference evapotranspiration rate (mm d⁻¹), $\lrcorner$ is slope of the saturation vapour pressure curve (kPa⁰C⁻¹), R_n is net radiation at the crop surface (MJm⁻²day⁻¹), G is soil heat flux density (MJ m² day⁻¹), γ is psychometric constant (kPa ⁰C⁻¹), T_{mean} is mean air temperature (°C), and u_2 is wind speed (m s⁻¹) at 2 m above the ground, e_s is mean saturated vapour pressure kPa), e_a *is* actual vapour pressure (kPa).

Potential evaporation (Ep) was calculated based on the function of ET_0, Leaf Area Index (LAI) and a constant radiation extinction (k) by canopy of 0.463 (equation 12). Since alfalfa is mainly grown in the field of the experimental sites, and depending on the time period of the study, crop height of 10 cm and constant rooting depth of 30 cm was defined in the model to estimate LAI. Actual evaporation (Ea) was generated by HYDRUS based on calculated potential evaporation and soil water content.

$$LAI = 1.5 \times \log(crop\ height) + 5.5 \qquad \textit{Eqn. 12}$$

$$E_p = ET_0 \times e^{-kLAI} \qquad \textit{Eqn. 13}$$

4.5.6. Root water uptake

Root water uptake (RWU) is considered as a sink term in HYDRUS, where actual transpiration (Tp) from crop is equal to water uptake by roots. It is the volume of water removed from a unit volume of soil per unit time due to water uptake by crops (Šimůnek e *al.*, 2013). RWU is dominantly correlated to water content and root vertical growth (Wang, Song, Wei, & Shao, 2016). Considering the constant root depth over the study period, actual transpiration from crop in HYDRUS was estimated based on Feddes et al. (1976) equation (Eqn. 14).

$$S\,(z,t) = \, \alpha\,(h,z)\beta(z)T_p \qquad \textit{Eqn. 14}$$

where, α is the dimensionless root water uptake stress response function at prescribed soil water pressure head (h); $\beta(z)$ is the spatial distribution function of root water uptake distribution (cm^{-1}); T_p is the potential transpiration from crop (mm).

Table 6 provides the parameters for water stress response function defined for alfalfa. Water uptake from roots of alfalfa is considered optimal between pressure heads Popt (-25cm) and P2 (-1500 cm) and changes linearly with pressure heads between P2 and P3 (or P0 and Popt). Water uptake is zero for pressure head less than the wilting point (P3=-8000cm), and also assumed to be zero when close to saturation point (P0).

Table 6: Root water uptake parameters considered for alfalfa in HYDRUS (based on Taylor and Ashcroft, 1972)

P0 [cm]	-10
Popt [cm]	-25
P2H [cm]	-1500
P2L [cm]	-1500
P3 [cm]	-8000

4.5.7. Model calibration

Model calibration is defined as fine tuning of model parameters to match the model output with the measured field data for the selected period and situation entered to the model (Rientijes, 2015). Model calibration was first performed in heterogeneous soil layer of 6 materials in PEW with atmospheric boundary condition with surface layer at top and constant flux of zero as a bottom condition. This heterogeneous layer was defined based on field observation and measurements in the laboratory. The soil hydraulic parameters were calibrated against water content measurements in the soil for the period of 25th Sept to 5th Dec 2018 in PEW site. The model was initially run using the inbuilt in Rosetta database (sand%, silt%, clay%, BD) for defining SHPs. Then trial and error approach was used, while staying within the pre-defined range of SHP estimated from different PTF as shown in Table 5 until the best fit of the measured water content data was obtained.

However, the model calibration in the PEW site was a daunting task. There were events of rainfall recorded in site but the soil moisture sensors failed to detect that moisture until 25th November as shown in Figure 9, where the sudden jump in water content from 0.09 to 0.16 cm^3/cm^3 was observed at the top 5 cm layer. As the top layers are highly variable, the measurements obtained were a bit unrealistic. The reason for this is that there was an error in the experimental set up of the sensors that was recognized only at the end of the observation period. A few days after the sensor installation, the local farmer, by mistake, put an extra layer of soil on the top of the experimental area. This extra layer of about 30-40 cam added on top (Figure 13) was not fully compact. In case of a high rainfall event, water could pass through the cracks relatively quickly, but low-intensity short rains were buffered in this layer.

To account for this error, an extra 30 cm layer was added on top of the previously defined soil profile of 310 cm i.e. a 340 cm deep soil profile was modelled. Calibration was performed by making this extra layer coarser than
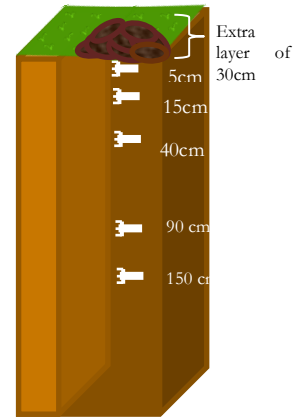
Figure 13: Experimental set up in study site

the ones below, so that the water is transported through to layer underneath, as it was observed. SHP of the top three materials (extra layer, silty clay and clay) were found to be most sensitive during the calibration process. SHP such as Ksat, θr, and α were mostly adjusted during the calibration process (Table 7) to obtain the best fit to the measured data. The calibrated model was then used back in time with the changes in forcing component i.e. 25th Sept 2015 to 28th Mar 2016 to simulate the ponding process. The outputs produced were validated based on the timing of ponding mapped from the Sentinel-1A images. For the initialization of SWC at selected nodes during the validation period, measured SWC values in the dry period of 25th Sept to 5th Dec of 2018 were used.

Table 7: Calibrated soil hydraulic parameters during calibration process in PEW site

Depth [cm]	Soil profile	θr [cm^3/cm^3]	θ_S [cm^3/cm^3]	α [cm^{-1}]	n [-]	Ks [cm/day]	L
0-30	Coarse soil	0.002	0.42	0.0001	1.156	10.96	0.5
30-35	Silty clay	0.002	0.2	0.0056	1.29	1.48	0.5
35-130	Clay	0.095	0.5	0.015	1.3	0.3	0.5
130-150	Silty loam	0.0686	0.45	0.0006	1.6149	10.96	0.5
150-230	Silty clay loam	0.085	0.52	0.0084	1.4872	6.01	0.5
230-250	Sandy loam	0.0581	0.42	0.0283	1.6087	54.83	0.5
250-340	Silty clay	0.0997	0.5	0.0132	1.3614	8.62	0.5

Considering the unknown GW table in NPEW area, a free draining lower boundary condition was set. The upper boundary condition was set to atmospheric boundary condition with surface runoff, considering the slope of the terrain that might contribute as runoff to PEW area. Due to the problem in the experimental setup (extra layer on the top), additionally a failure of the 5 cm sensor and unrealistic values provided by the 120 cm sensor at this site, the model in NPEW could not be calibrated. Nevertheless, experimental model runs were made. SHPs were assigned based on neural network predictions (% of sand, silt, clay and BD) as shown in Table 8 and the model was used to simulate the SWC for the period of 25th Sept. 2015 to 28th Mar. 2016 with the initial value taken from the 2018 data of the remaining good sensors at the NPEW site.

Table 8: Soil hydraulic parameters for NPEW site

Depth [cm]	Soil profile	θr [cm³ cm⁻³]	θS [cm³ cm⁻³]	α [cm⁻¹]	n [-]	Ks [cm day⁻¹]	L
0-5	Silty clay	0.1036	0.4868	0.0178	1.2348	7.15	0.5
5-15	Silty clay loam	0.0903	0.4544	0.0178	1.2348	6.69	0.5
15-80	Silty clay	0.0981	0.4657	0.0149	1.296	4.88	0.5
80-100	Clay	0.1031	0.4994	0.0171	1.2751	8.19	0.5
100-120	Silty clay	0.1036	0.4868	0.0178	1.2348	7.15	0.5
120-190	Sandy loam	0.0952	0.4244	0.0179	1.2016	4.62	0.5
190-280	Silty clay	0.0986	0.4863	0.0134	1.3521	8.95	0.5

Summarizing the above process, following cases were defined.

Case 1a: Model calibration for the year 2018 (25th Sept to 5 Dec) in PEW location

Case 1b: Simulation in the year 2015 to 2016 (25th Sep to 28th Mar) in PEW location

Case 2a: Simulation in the year 2015 to 2016 (25th Sep to 28th Mar) in NPEW location

4.5.8. Performance indicators

The performance of a model is assessed using corresponding measured and simulated variables. The evaluations in this study were however focusing on soil water content values at selected depths. Simulated water content by HYDRUS for the period of 2018 was compared with measured water content at selected nodes in the field. Performances were first assessed via. visual inspection of measured and simulated values that allowed quick assessment of the model fit and the biases observed during calibration. Errors were then quantified and evaluated using mean error (ME), mean absolute error (MAE), root mean square error (RMSE) and index of agreement (d-index) by Willmott et *al.*, (1985). ME (Eqn. 15) provided the bias between the modelled and observed values, i.e. the over or underestimation of water content in the calibrated model. While the magnitude of the error was measured by the MAE (Eqn. 16) and RMSE (Eqn. 17). On the other hand, d-index (Eqn. 18). was used to assess the fit of the time series graphs of the simulated and measured water contents. Low values of ME, MAE and RMSE indicated a good fit between simulated and measured values. A d-index of $0 \leq d \leq 1$ indicates the goodness of fit. Closer the value is to 1, the more accurate the model prediction is and vice versa.

$$ME = \frac{1}{n}\sum_{i=1}^{n}(\theta_m - \theta_c)_i \qquad \text{Eqn. 15}$$

$$MAE = \frac{1}{n}\sum_{i=1}^{n}|\theta_m - \theta_c|_i \qquad \text{Eqn. 16}$$

$$RMSE = \sqrt{\frac{1}{n}\sum_{i=1}^{n}(\theta_m - \theta_c)_i^2} \qquad \text{Eqn. 17}$$

$$d = 1 - \frac{\sum_{i=1}^{n}(\theta_{m,i} - \theta_{c,i})^2}{\sum_{i=1}^{n}(|\theta_{m,i} - \overline{\theta_c}| + |\theta_{m,i} - \overline{\theta_c}|)^2} \qquad \text{Eqn. 18}$$

$$RVE = \left[\frac{\sum_{i=1}^{n}Q_{m(i)} - \sum_{i=1}^{n}Q_{c(i)}}{\sum_{i=1}^{n}Q_{m(i)}}\right] \times 100 \qquad \text{Eqn. 19}$$

Where, n is the number of calibrated values, θ_m is the measured soil water content from field (cm³/cm³) and θ_c is the calculated soil water content by the model (cm³/cm³).

4.5.9. Water balance closure

Water balance (WB) is the change in the volume of water within the flow domain to the net flow across domain boundaries including RWU during entire simulation (Šimůnek et *al.*, 2013). It was also used to assess the discrepancy between total inflow and outflow. In HYDRUS, WB is computed according to prescribed time and sub-regions defined, where each sub-regions consisted actual volume of water (V) and inflow or outflow rate (O,) from the sub-region (equation).

$$V = \sum_e \Delta x_i \frac{\theta_i + \theta_{i+1}}{2} \qquad\qquad \textit{Eqn. 20}$$

$$O = \frac{V_{new} - V_{out}}{\Delta t} \qquad\qquad \textit{Eqn. 21}$$

Where, θ_i and θ_{i+1} are the water contents at the corner nodes of element e, Δx_i is the size of the element, V_{new} and V_{old} are volumes of water in the sub-region computed at the current and previous time step.

The relative error of the mass balance of the flow domain was calculated as:

$$\varepsilon_r^w = \frac{|\varepsilon_a^w|}{max\left(\sum_e |V_t^e - V_0^e|, \int_0^t T_a dt + \int_0^t (|q_N| + |q_0|) dt\right)} \qquad\qquad \textit{Eqn. 22}$$

Where, ε_a^w is the absolute error of mass balance V_t^e and V_0^e represents the volume of water in element 'e' at time 't' and 'zero' respectively; T_a represent cumulative root water uptake amount, q_N and q_0 are the net cumulative fluxes through both boundaries. The first term in denominator indicates the sum of the absolute changes in water contents over all elements, second term represent the sum of the absolute values of all fluxes in and out of the flow domain.

5. RESULT AND DISCUSSION

5.1. Soil Physical Parameters Analysis

5.1.1. Particle size analysis

The particle size distribution (PSD) was determined based on the percentages of clay, silt and sand in the laboratory. Figure 14 and Table 9 show the particle distribution and the soil texture distribution in the two modelled profiles at the inundated and non-inundated sites. A clear vertical differentiation in the properties of soil was found in two different locations. The PEW site was characterized by the presence of predominant fine-grained clay soils (<2 µm) which ranged from 51 % to 59 % till 1m. In the NPEW area, the soils were more composed of silty clay (20-50 µm) from 40 to 80 cm and ranged from 51 % to 56 %. Sample from PEW in plot 2 (Bore 1) was also characterized by higher clay deposition from 30-150 cm in the soil profile. The top layer was however composed of silty clay that varied in thickness in all the areas. This variation in top layer was because they are mostly plowed for cultivation. Low fraction of sand was observed throughout the soil profile except at the depth of 220 cm and 190 cm in PEW and NPEW sites respectively.

Measured PSD was compared with SoilGrids250m (SG) data. The outputs of SG data was incomparable to the ground truth data. Clay loam was predicted by SG in all three locations at all depths (0, 5, 15, 30, 60, 100, 200 cm). Clay fractions were largely underestimated and sand fractions were overly estimated. SG data did not reflect the differences as observed in inundated and non-inundated sites and therefore, the dataset was not applicable to study ponding water issues. More representative sample points with respect to depth from inundation prone areas should be taken to improve the available dataset.
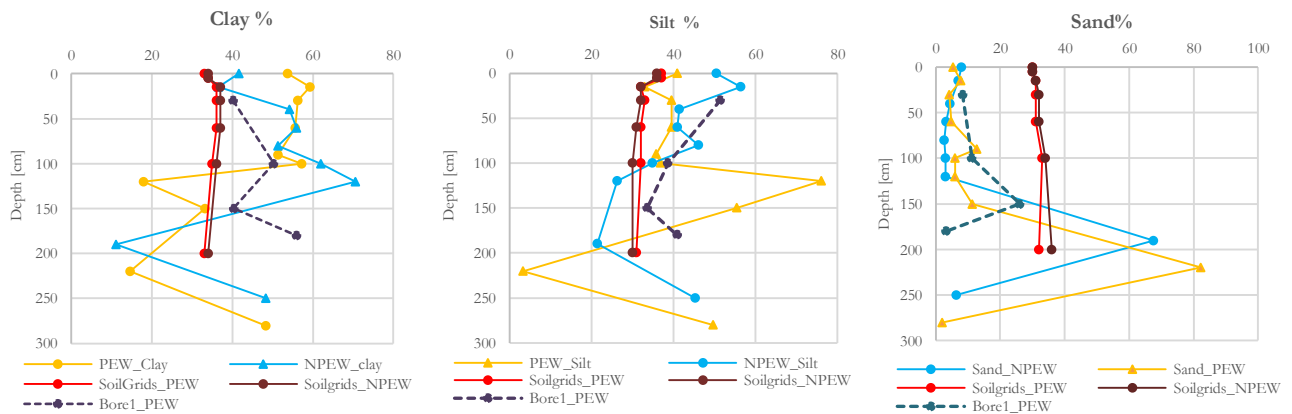
Figure 14: Particle size distributions in the experimental site

PEW studies are extensive in southern parts of Hungary. Heavy, non-calcic clay and clay loam soil was noted in Southern PEW sites of Hungary (Barta, 2013). Gál & Farsang (2013) found silty clayic loam and silty loam soil in respective inundated and non-inundated sites of southern Great Hungarian Plain. The difference in texture is possible because of the inheriting characteristics from the parent rock. Moreover, on an average higher proportion of clay (26.16-45.47%) was found in PEW than in NPEW (21.02 to 33.49%). The proportion measured in Northern site was much higher compared to the southern site, but clay deposition in inundated sites was comparable. Fine layer deposition followed by coarse layer in the depression could be attributed to very slow settling time for fine soils. Continuous inundation in the area

consequently resulted in the development of a thick layer of fine material. According to Kuti et al. (2006) surface permeability, near-surface geological formation and hydrostatic level of groundwater play a decisive role in PEW formation. Finer particles like clay and silt fraction are recognized to be favourable for the PEW formation (Barta, et al., 2013; Gal, 2013; Van Leeuwen et al., 2016). Because of the high retention property and low permeability (Kuti et al., 2006) of clay soils, it can either delay or prevent the infiltration process thereby causing the risk of inundation. It was also noticed that few UDSS took 3-5 weeks to saturate in the laboratory, and big swellings were also found during the period. This suggests that the material present in the inundation area is nearly impermeable and that it aids in the development of ponding. Additionally, this impervious layer coupled with other factors such as low depression in the area that accumulates and retain water, meteorological factor and compaction could also trigger in the formation of excess water.

5.1.2. Bulk density, porosity, organic carbon, soil water content

Table 1 compares the distribution of mean BD, porosity, OC and SWC in different sites and according to depth. In both locations, the increasing tendency of BD with respect to depth was measured. However, the magnitude was slightly higher in the case of PEW than in NPEW. It ranged from 1.154-1.63 g cm^{-3} in PEW, 1.36-1.58 gcm^{-3} in NPEW and 1.365 to 1.442 gcm^{-3} in PEW of plot 2. Based on UDSS, measured BD was highest for silty clay loam (1.58 gcm^{-3}) at a depth of 150 cm. On the contrary, it was largest for silty clay (1.467 gcm^{-3}) at a depth of 60 cm. Moreover, BD estimated based on Cosby et al. (1984) and Hillel (2003) showed the highest BD for sandy loam soils in both sites. Higher (1.44 and 1.51 gcm^{-3}) and increasing BD with depth was also noted in inundated areas than in non-inundated areas (1.45-1.48 gcm^{-3}) of Békés County, in the Southern Hungarian Great Plain (Gál et al., 2017).

Porosity which was estimated from BD showed an inverse relationship to BD. It decreased with depth in both sites. High porosity was measured in PEW, which ranged from 0.38 to 0.57 than in NPW area (0.403-0.485). High porosity was measured near the surface layer in both sites, which peaked again at 100 cm. This is plausible to the field observation, where 30-40 cm of the soil profile is generally ploughed and during measurement, this layer was composed of drier angular soil aggregates. As a result, low BD is measured in the top layer. However, at a depth of 100cm increased porosity was mainly due to high clay mineral composition of 57.22 % and 62.024 % in PEW and NPEW respectively. Lowest porosity was measured at depth of 220 cm and 190 cm which were both composed of sandy loam in PEW and NPEW area. Porosity is inversely proportional to grain size. Small particle size with the greater volume of pore spaces is the characteristics of fine or clay soils than the coarser or sandy soils.

Organic carbon (OC) measured in the laboratory is different from organic matter that includes all the elements such as hydrogen, oxygen, nitrogen etc. Organic matter (OM) was estimated from OC with a conversion factor of 1.7 as given by Weil & Brady, (2016). OM in PEW ranged from 0.65 -5.6 % and it was 2.5-8.8% in NPEW which dipped down with depth in both locations. Though the percentage was very low, they were more present at the surface layer of 0-15cm. The higher fraction was also found in the deeper layer of 150 cm (5.51%) and 120 cm (8.8%) in PEW and NPEW respectively. High OM content was found in NPEW than PEW area. Low OM content (1-2 %) was also measured in PEW sites between South Tisza valley and Marosszög (Barta, 2013).

Table 9: Measured soil parameters in laboratory

Site	Sample	Depth	Texture	BD	Porosity	OC [%]	K_{sat} [m/s]	ISWC [cm³/cm³]	Sat. SWC [cm³/cm³]
PEW	DSS	0	Silty clay	1.372	0.482	2.91			
	UDSS	15	Clay	1.154	0.565	3.34	3.03E+01	0.160	0.319
	UDSS	30	Clay	1.458	0.450	1.36	3.42E+01	0.177	0.282
	UDSS	60	Clay	1.495	0.436	1.02	2.36E+01	0.172	0.256
	DSS	90	Clay	1.485	0.440	0.78	2.89E+00	0.167	0.264
	DSS	100	Clay	1.374	0.481	0.85			
	UDSS	120	Silt loam	1.517	0.428	0.62	9.14E+00	0.174	0.293
	UDSS	150	Silty clay loam	1.580	0.440	3.24	6.67E-02	0.169	0.237
	DSS	220	Sandy loam	1.630	0.385	0.38			
	DSS	280	Silty clay	1.361	0.486	1.62			
NPEW	DSS	0	Silty clay	1.381	0.479	3.34			
	UDSS	15	Silty clay loam	1.441	0.456	2.7	2.77E+01	0.106	0.240
	UDSS	40	Silty clay	1.439	0.457	2.32	4.33E+01	0.128	0.263
	UDSS	60	Silty clay	1.467	0.446	2.81	2.02E+01	0.153	0.267
	UDSS	80	Silty clay	1.448	0.453	3.21	5.11E-01	0.173	0.279
	DSS	100	Clay	1.364	0.485	2.8			
	UDSS	120	Clay	1.396	0.473	5.18	3.40E-01	0.183	0.268
	DSS	190	Sandy Loam	1.581	0.403	1.52			
	DSS	250	Silty clay	1.376	0.481	1.61			
Bore 1	UDSS	30	Silty Clay	1.382	0.478	2.46			
	UDSS	100	Clay	1.392	0.475	0.87			
	UDSS	150	Clay	1.442	0.456	0.36			
	UDSS	180	Silty Clay	1.365	0.485	0.37			

BD is taken as an indicator of soil health and compaction. It is affected by changes in OM, soil texture, PSD, porosity, water, root penetration, land use, and management (Tanveera, Kanth, Tali, & Naikoo, 2016; Chaudhari, et *al*, 2013) . BD generally increases with profile depth due to compacted subsurface layer, low OM content, and porosity. BD of sandy soils is usually larger (1.37-1.7 g/cm³) than fine silt and clay soils (1.1-1.6g/cm³) [8] due to differences in pore space between these soils. Finer particles are very small and can have a greater volume of open spaces where many small pore spaces fit between them. BD is also an indicator of compaction. In Heves County, high compaction close to the surface condition with >60% harmful compaction [9] had been reported. Formation of compact layer had been measured in other inundated sites (Gál & Farsang, 2013; Barta et al., 2013) which was attributed to natural (continuous inundation) and human causes (agricultural machines). Though compaction was not measured in the field, clay soils coupled with several factors such as topography, and meteorological factor indicates that the area is susceptible to inundation problem.

Reduction in BD was strongly correlated with OM as shown in Figure 15. The rate of fall was sharper in NPEW where comparatively high OM was found. The strong negative correlation between OM and K_{sat}

---

[8] http://soilquality.org.au/factsheets/bulk-density-measurement
[9] http://okir-tdr.helion.hu/?diapoly=4.2.1

has been reported in many studies (Nemes, Rawls, & Pachepsky, 2005; Jana, Mohanty, & Springer, 2007). OM is generally more porous than mineral soil particles, which present in soil enhances infiltration. On the other hand, soils with less OM content creates less pore space between soil particles (Bot & Benites, 2005) that can more easily create a compact layer, and thus increasing the risk of PEW formation.
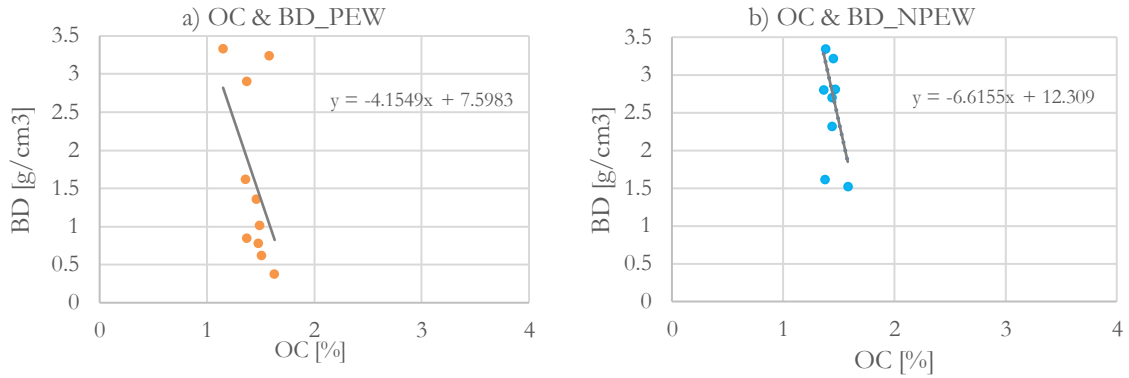
Figure 15: Correlation between organic carbon and bulk density in PEW (a) and NPEW (b) area of plot 1

The initial soil water content (ISWC) and saturated soil water content (SSWC) of UDSS was measured based on a weight basis. Results in Figure 15 showed increasing field moisture condition and decreasing SSWC with respect to depth in PEW. In NPEW, both ISWC and SSWC increased with depth. The increasing trend of ISWC corresponds to sensor measurement (Table 3) but the difference in magnitude was quite low compared to sensor measurement. The increasing trend was more pronounced in NPEW, but have slightly low moisture content than PEW. The error of low moisture content measured was because of delayed measurement in laboratory i.e. after three weeks where available moisture might have evaporated.

SSWC is defined as the maximum amount of water a soil can store and is related to total soil porosity. SSWC measured clearly does not correspond to measured porosity. The error could be because of the air entrapped in the pore space or also error in the samples taken itself. Nevertheless, the calculated SSWC showed more variation in moisture content especially at a depth of 15-90 cm where clay soil is present. The decreasing tendency of SSWC also indicates the low permeability within the clay layer. In NPEW, consistent and slow increase in SSWC with depth was observed.
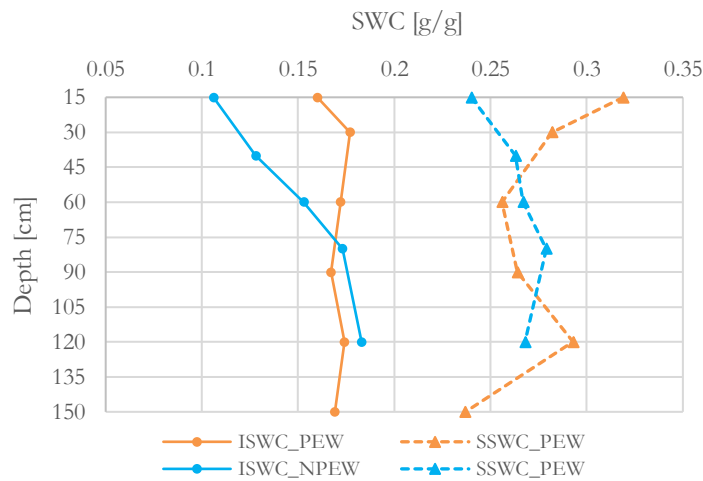
Figure 16: Initial (ISWC) and saturated water content (SSWC) calculated on weight basis in PEW and NPEW site

5.1.3. Saturated Hydraulic conductivity

K_{sat} describes the saturated soil pores ability to transport water which is affected by soil pore geometry, fluid viscosity and density[10]. Measured K_{sat} of UDSS in the laboratory using the constant head method showed a decreasing trend with respect to depth in both sites (Figure 17). The measured K_{sat} values do not correspond to the different texture measured at respective depth in the PEW area. It was more related to measured BD and porosity of the soil sample. With increasing depth and BD, K_{sat} decreased and it increased with larger porosity. It was also noticed that with the same textural class, K_{sat} varied significantly, which might have been influenced by the structure of the soil (Haghnazari, Shahgholi, & Feizi, 2015).

Huge error in terms of the magnitude of K_{sat} was measured. According to soil parameters measured in Oregon State University Land-surface Model (OSU LSM) in Hungary and USA, K_{sat} for clay was 8.0×10^{-7} m/s and 9.74×10^{-7} m/s respectively. Similarly, for silty clay, it was 1.05×10^{-7} m/s and 1.34×10^{-7} m/s for respective countries (Horváth, Ács, & Breuer, 2009). The measured dataset in the laboratory was 5-7 order of magnitude higher than the referenced one and with one also established from different PTFs (Table 5). The possible reason for the error could be related to field and laboratory experiment. Presence of roots in the sample ring, cracks developed, the longer time period of saturation, swelling of clay soils, difficulty in achieving a steady state condition during measurement, the limited number of samples (2 per depth) collected could be attributed to uncertain error in measured K_{sat}. Furthermore, clay minerals with semctite show a strong swelling property that changes with seasonal moisture conditions (Barta et al., 2013). This swelling property reduces the hydraulic conductivity by blocking the pores and during dry period the cracks developed enhances the permeability (Adamcova et al., 2005). This swelling nature of soil was experienced in the laboratory that increased with depth. Presence of angular clay soils till a depth of 40 cm was also observed during sample collection in dry period. The error introduced in laboratory measured could be because of such nature of soil observed in the area.

Infiltration largely depends on hydraulic conductivity of the soil. High conductivity will cause a high amount of rainfall to infiltrate into the soil and vice versa. The measured extreme conductivity value in the laboratory could significantly produce an erroneous result. For this reason, the incomparable K_{sat} with respect to the one estimated from different PTFs (Table 5) was further not applied for modelling purpose. A range of uncertainty defined based on different PTFs that included texture, particle size, BD, porosity and organic matter (Table 5) was applied for modelling purpose.
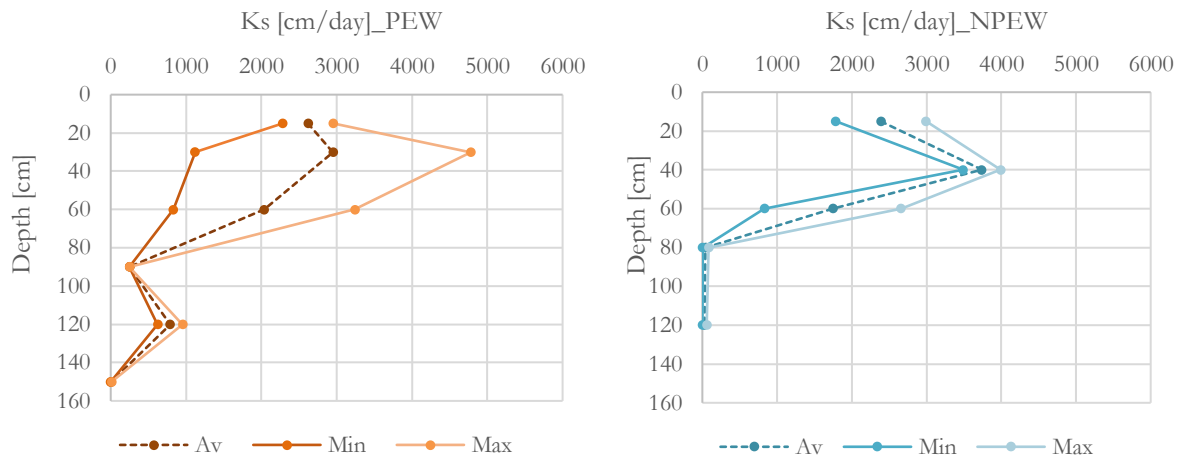
Figure 17: Measured saturated hydraulic conductivity of UDSS with respect to depth

---

5.2. Calibration Results

5.2.1. Meteorological Characteristics

Calibration of the model was performed for the period of 71 days i.e. 25th Sep to 5th December 2018. The meteorological conditions during the calibration period are shown in Figure 18. The measured total precipitation based on Bogas station was 88.90 mm. The daily maximum amount of rainfall was recorded as 15.80 mm in November. The number of rainy days during the study period was 24. The total accumulation of rainfall was greater during November-December (60.4 mm) than September-October (28.5 mm). The average temperature during the period was 8.0 ^{0}C, and it dipped down to the lowest of -6.90 ^{0}C in December. The average recorded sunshine hours, wind speed and relative humidity recorded were 4.2 hr, 1.04 m/s, 71.5 % respectively.
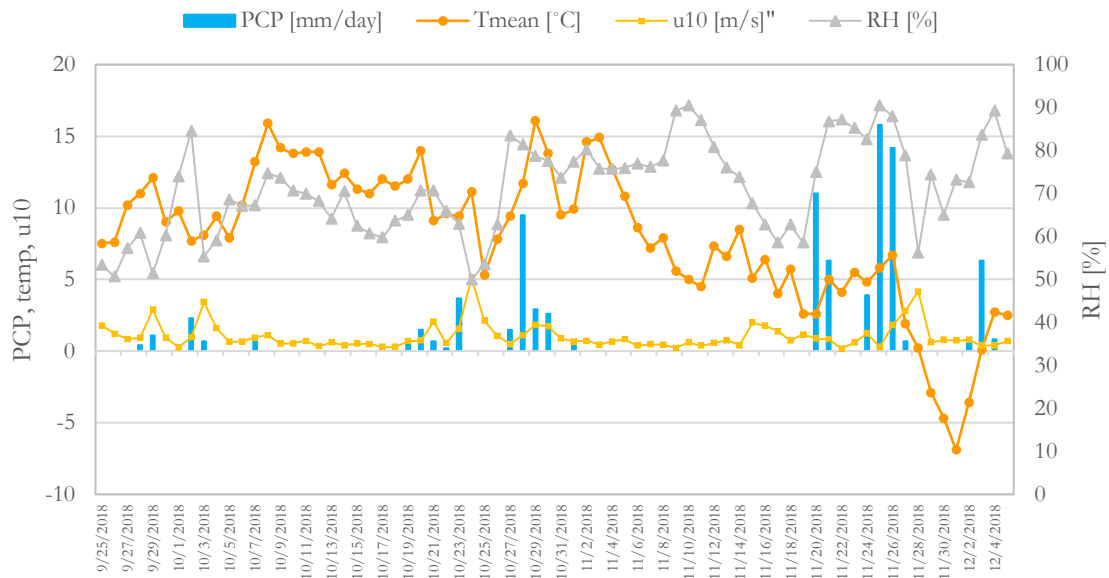
Figure 18: Time series of meteorological parameters during calibration period

5.2.2. Model calibration

Case 1a: Model calibration in the year 2018 (25th September to 5th December) in PEW location

The model calibration was based on field measurements of soil moisture at selected depths in a non-uniform soil profile of 340 cm under a time-variable forcing conditions. The time-depended soil volumetric water content at five different depths of (+30) 5, 15, 40, 90, 120 and 150 cm was simulated based on calibrated soil hydraulic parameters (Table 7) is shown in Figure 1. The average SWC measured at the respective depths were 0.09 (0.07-0.22), 0.11(0.09-0.18), 0.34 9 (0.31-0.35), 0.43 (0.40-0.44), 0.49 (0.47-0.50) cm³/cm³.

Table 10: Performance indicators of simulated soil water content at different depths

Error indicator	5 cm	15 cm	40 cm	90 cm	150 cm
ME [cm³/cm³]	0.012	-0.016	0.014	0.018	0.0018
MAE [cm³/cm³]	0.03	0.02	0.02	0.01	0.01
RMSE [cm³/cm³]	0.0253	0.0287	0.0133	0.0153	0.0060
d-index	0.9130	0.8549	0.5026	0.4917	0.4281
RVE [%]	20.86	-16.71	5.60	2.72	-1.04

Visually, the simulated water content showed good agreement with the measured SWC at all depths. Statistically, the d-index value showed that the SWC at a depth of 5 and 15 cm in very good agreement with the measured SWC and with poor agreement at deeper levels of 40, 90 and 150 cm (Table 10 and Figure 19). However, the relative volumetric error (RVE) and MAE decreased with increasing depth. Large error at the surface layer (5, 15 cm) was because it was affected by evaporation and root water uptake (Zheng et al., 2017). The assumption of uniform plant root distribution up to the 30 cm depth and crop height of 10 cm throughout the simulation period could be one of the reasons for the discrepancy. Parameterizing the process with an extra layer added on top of the surface layer, and the dynamics of cracks developed (formation, closure, shifting) that could have led to preferential flow down the layer underneath (Greve, Andersen, & Acworth, 2010) can be attributed to error measured at 5-15 cm. Underestimation (0.012 cm^3/cm^3) occurred in the first layer for a longer period until the peak observed at the end of November. Despite the addition of an extra layer of soil in the profile studied, the incoming flux was fairly translated in terms of soil-water transport nearly at the end of the simulation period. The major peak of 0.22 cm^3/cm^3 and the falling and thereafter rising limb was well represented by the model. However, overestimation of the rising limb in the form of a small peak was observed. This could be related to the two days antecedent rainfall (17.3 mm) that was transported with a one day lag. Overall, the shape of the fluctuation measured was well captured by the model, which is evidenced by a d-index value of 0.91. Similarly, for the second layer, slight overestimation of -0.016 cm^3/cm^3 was observed but in overall was well simulated by the model (d-index=0.85). Large overestimation was mainly observed on 27th November. The peak measured was delayed by a day before and also the dynamics after that was not well represented.

Water transport through the soil layer is strongly controlled by soil hydraulic parameters. It is difficult to define a single set of parameters that could accurately represent the transport process in a heterogeneous soil column. A single set of parameter was applied to a large thickness of clay and silty clay layer present in PEW and NPEW respectively, and that have different properties (BD, porosity, OC, PSD) within the same textural classes. During calibration, the top two layers reacted in a highly variable way to the changes made in SHP. Water transport through these two layers was strongly influenced by the extra layer added at the top. The conductivity value and available water content had to be increased to mimic the measured water content at 5 cm which was a silty clay layer. Since the measured differences in SWC of 5 cm and 15 cm was very small (0.02 cm^3/cm^3) the conductivity values had been lowered down significantly to get the best fit.

For the bottom three layers, the fluctuations in measured SWC was very small, but it showed a tendency of low SWC at the starting period and then dropping further at the end of the measurement time period. Such a trend, however, was not captured by the model and is indicated by the large discrepancy of d-index of 0.50, 0.49 and 0.42 at a depth of 40, 90 and 150 cm respectively. Simulated SWC values were slightly underestimated by 0.014, 0.018 and 0.0018 cm^3/cm^3 in the respective depths of 40, 90 and 150 cm and the RMSE also ranged from 0.0060-0.0153 cm^3/cm^3. The measured mean and RMSE and RVE were lowest for the deepest profile (150 cm) but it was represented with a poor d-value. The discrepancy was mainly observed in the start and at the end of the simulation period. The sudden rise in the start of the measured SWC values (0.48 to 0.499 cm^3/cm^3) until it stabilized to a nearly constant SWC of 0.499 cm^3/cm^3 after 6 days was not captured by the model. This low value in the starting period could be explained by error induced during installation of sensors. Two pits were dug in the site, where the first set of sensors were installed in NPEW site in day 1 and another set in PEW site in day 2. The pit in the site was dug during the morning period and the sensors were installed nearly at sunset. The exposure of the soil profile throughout the day (nearly 2 days) in PEW might have evaporated the water content. The consistent small drop could also be seen at a depth of 40 and 90 cm. As a consequence low initial value was measured resulting in a poor

simulation. Despite the magnitude of errors measured, the calibrated SHP were used for simulation of ponding, which was validated with the satellite images at the same time period.
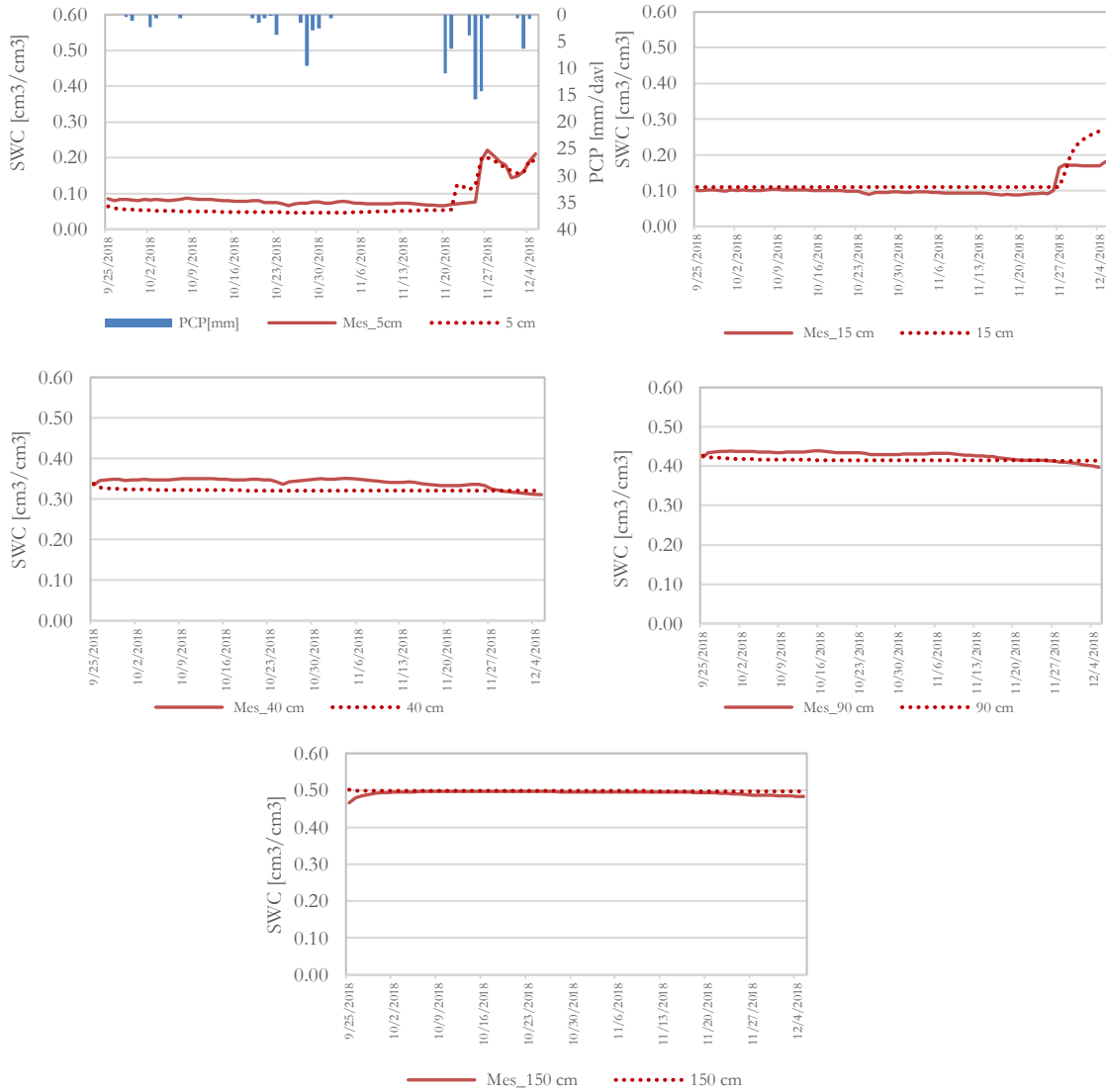
Figure 19: Comparison of measured and simulated soil volumetric water content at selected depths of 5, 15, 40, 90 and 150 cm

5.3. Ponding and runoff simulation and validation with satellite

Case 1b: Simulation in the year 2015 to 2016 (25th Sep to 28th Mar) in PEW location

5.3.1. Meteorological characteristics

Calibrated parameters were applied for the period of 186 days i.e. 25th Sep 2015 to 28th March 2016 with in the corresponding forcing components. The meteorological conditions during this simulation period are shown in Figure 20. The total amount of precipitation recorded during the period was 294 mm, which is three times larger than the rainfall in the calibration period (88.90 mm). The total number of rainy days was 62 (33.3%). The daily maximum amount of accumulation was about 28 mm (10/16/2015). Two major peaks of monthly rainfall were measured during October 2015 (88.4 mm) and February 2016 (82.7 mm). The lowest amount of rainfall was recorded during December (4 mm).

The average temperature was 3.92 ^{0}C with a range of -12.10 ^{0}C to 17.90 ^{0}C. The temperature started to decrease after mid-November 2015 and reached to lowest during January 2014 (-12.10 ^{0}C). On average it remained as low as 3.8 ^{0}C in February 2016 and increased to about 5.1 ^{0}C in March 2016. The average sunshine hour during the period was 3.55 hrs (0.07 to 7.54 hours) with the lowest observed during November to January. The average RH and wind speed measured was 76.16 % (39.33 to 90.83 %) and 1.12 m/s (0.08 to 4.55 m/s) respectively.
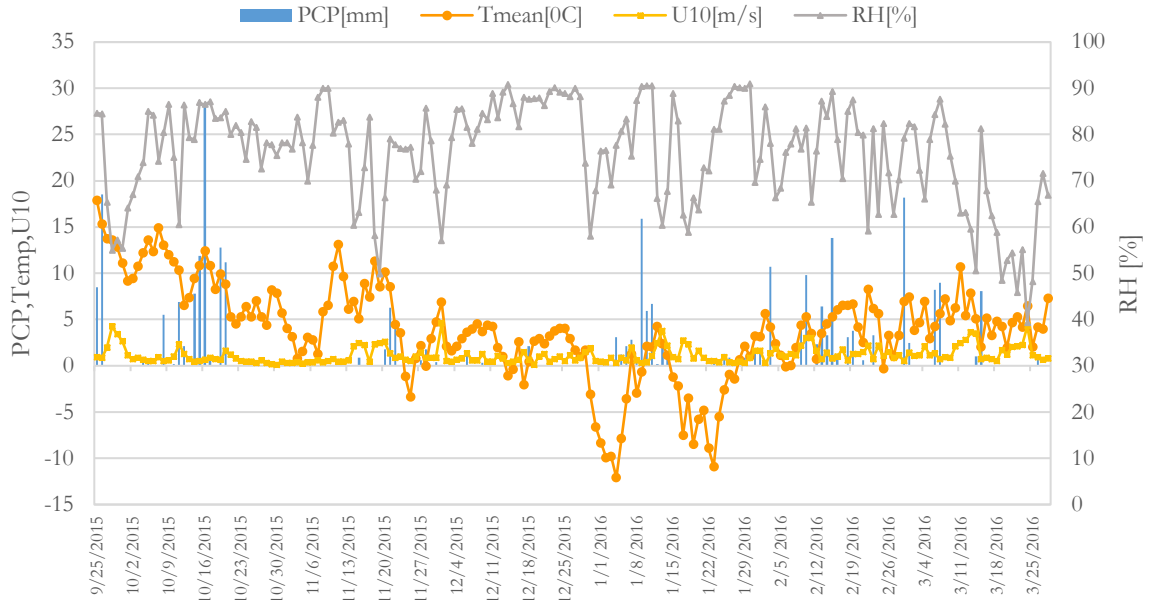
Figure 20: Time series of meteorological parameters during the validation period

5.3.2. Ponding simulation in PEW site

The calibrated model parameter was applied in different time window (25th September 2015 to 31st December 2015) in a heterogeneous soil profile of 310 cm under a time variable rainfall condition. During validation process, the extra top layer of 30 cm was removed and the SWC was simulated to the real profile observed in the field (6 layers). The SWC simulated as a function of time (186 days) is shown in Figure 21. The interest of simulation was from January to March 2016, where ponding was mapped from the satellite images (Figure 11), and the initial time period (25th Sep-31st December, 2015) of 98 days was taken as warmup period. Figure 20 provides the characteristics of SWC evolution with time. Instances of saturated conditions in the first (5 cm) and second layer (15 cm) was observed, which is represented by the flat horizontal line. The effect of variable ponded condition on third layer (40 cm) showed delayed response of infiltration. Deeper layers (90 and 120 cm) did not reach the saturation. This showed that the interlayer clay inhibited the water transport to the deeper layers.

Ponding usually occurs if the precipitation rates exceeded the K$_{sat}$ value, and water would start to accumulate to a certain height (Šimůnek et al., 2013). The storage capacity of soil at the beginning of the rainfall event is also a determinant factor for ponding or runoff process to occur. According to Miyasaka et al. (2017), the water flux into the soil is equal to rainfall intesity when it is less than the infiltration rate and that the soil hydraulic properties of the soil surface do not affect the water flux. Figure 21 and Table 11 analyzes whether excess water (or runoff) occurred during or after heavy rain in the field. It was observed that the ponded water condition simulated over time not only strongly corresponded to high rainfall events but also the antecedent prolonged rainfall events that saturated the soil and eventually allowed ponding on the surface. Since the hourly rainfall inputs were not available to analyze the impact of high intensity of rainfall, total

accumulation of rainfall in a day was used for analysis. It was observed that ponding was simulated in all three months. During 3 months, there was 42 % of rainy days and 38 % of ponding days (33 days) simulated by the model. Saturation point in the top layer was first reached after 5 rainy days followed by high daily rainfall of 15.9 mm that induced excess water formation. The condition shifted back to non-ponding state after 6 days when rainfall was ceased or when rainfall intensity was lower than infiltration rate. A maximum head condition of 1.016 cm was formed on the surface (Figure 21b). During this process, saturation in second layer (15 cm) reached after 4 days on ponding in top layer.

Frequent occurrences of ponding was observed in February, where 17 days of ponding was simulated by the model, followed by 10 and 6 days in March and January respectively. The maximum duration of 13 days of continued ponding was observed in February (9th-21st) with a least of one day accumulation also observed on 23rd February. A maximum head of 1.22 cm was established during the period (h=0.348-1.22 cm). It was noticed that heavy rains triggered the development of ponding as shown by the high starting rainfall value in Table 11. The number of rainy days in January (16 days, 46.3 mm) and February (15 days, 82.7 mm) were similar but the total daily rainfall in February was nearly twice the one measured in January. During March, the total accumulation was only 29.7 mm. Saturation in the second layer reached after two days. Besides heavy rain, longer duration of rainfall also contributed in excess water formation, as seen by frequent intense rainfall events in February. Frequent intense and longer duration of rainfall coupled with low temperature during winter and clayey nature of soil observed in the depression, neither allowing water to runoff nor to infiltrate at a high rate caused the excess water to pond at the surface (Barta et al., 2013).
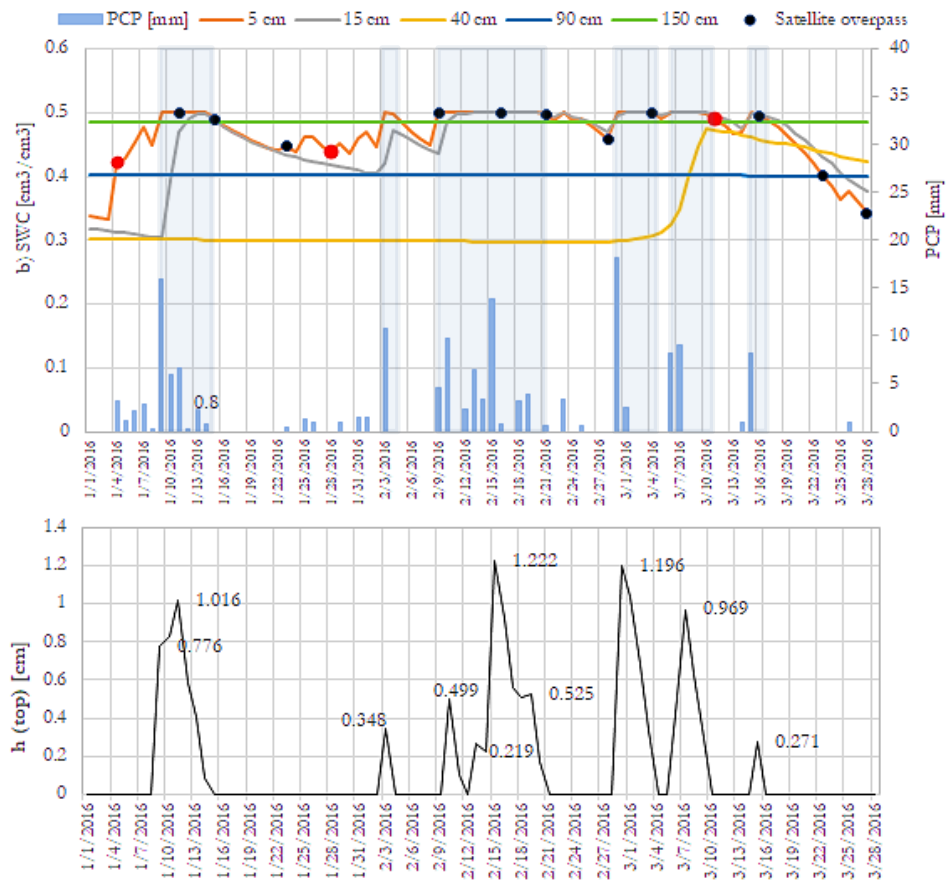

Figure 21: Time series of simulated SWC content for the period 2016 (a) and from January to March 2016 (b) head established during ponding period

Table 11: Ponding characteristics

Ponding period		No. of days of ponding	Rainfall [mm]		Max. ponding depth [cm]	Av. Infiltration rate [cm/d]	
Start	End		Total	Start of the ponding		PEW	NPEW
1/9/2016	1/14/2016	6	31.9	15.9	1.016	0.09	0.14
2/3/2016	2/4/2016	2	10.7	10.7	0.348	0.07	0.27
2/9/2016	2/20/2016	12	47.8	4.5	1.222	0.08	0.16
2/23/2016	2/23/2016	1	3.3	3.3	0.1	0.04	0.14
2/29/2016	3/4/2016	5	20.4	18.2	1.196	0.09	0.22
3/6/2016	3/10/2016	5	17.2	8.2	0.969	0.05	0.09
3/15/2016	3/16/2016	2	8.1	8.1	0.271	0.20	0.06

Infiltration, evaporation, root water uptake simulated by the model is shown in Figure 22. The average rate at which it infiltrates was 0.032 cm/d which is very low. This slow rate of flow is due to the clay layer underneath that impedes the downward flow. The cumulative infiltration measured during the study period was 15.56 cm (Figure 22g). The infiltration dynamics during the ponding period and the interaction between evaporation and RWU is shown in Figure 22a. It was observed that evaporation from soil was mainly active when there was no ponding in the area. Additionally, RWU from plants also was negligible during ponding period. When the incoming flux lowered, plants were under stress and they started to take up water from the soil. Evapotranspiration was prominent during end of the March when the site was exposed to negligible rainfall and increased warming. SWC also decreased with time with increased ET. The actual evaporation during January-March 2016 was measured as 0.29 cm and transpiration from plants was 10.553 cm. The water loss in the form of evapo-transpiration accounted to 68.33 % of infiltration amount. Also 31.8% of infiltration amount water was attributed to storage (5.05 cm).

Based on the calibrated model, the ponding depth simulated by the model only ranged from 0.1 to 1.222 cm (Table 11) which is very less. According to the farmer, the ponding depth in the site could reach to 100 cm. The simulated ponding depth was compared with the depth estimated based on drone derived DEM and Sentinel 1A images (Table 12). It was observed that the depth of the accumulation in the area could be between 28 to75 cm (Table 12). It also showed the decreasing depth of accumulated water over the time. Such differences indicated that either the rainfall data used was not representative of the area or the model was not well calibrated. Low infiltration rate measured and depth estimated by DEM also suggested that the available calibration of the data was far too little and that the infiltration might still be overestimated. Lower Ksat value might be required to further calibrate the model.
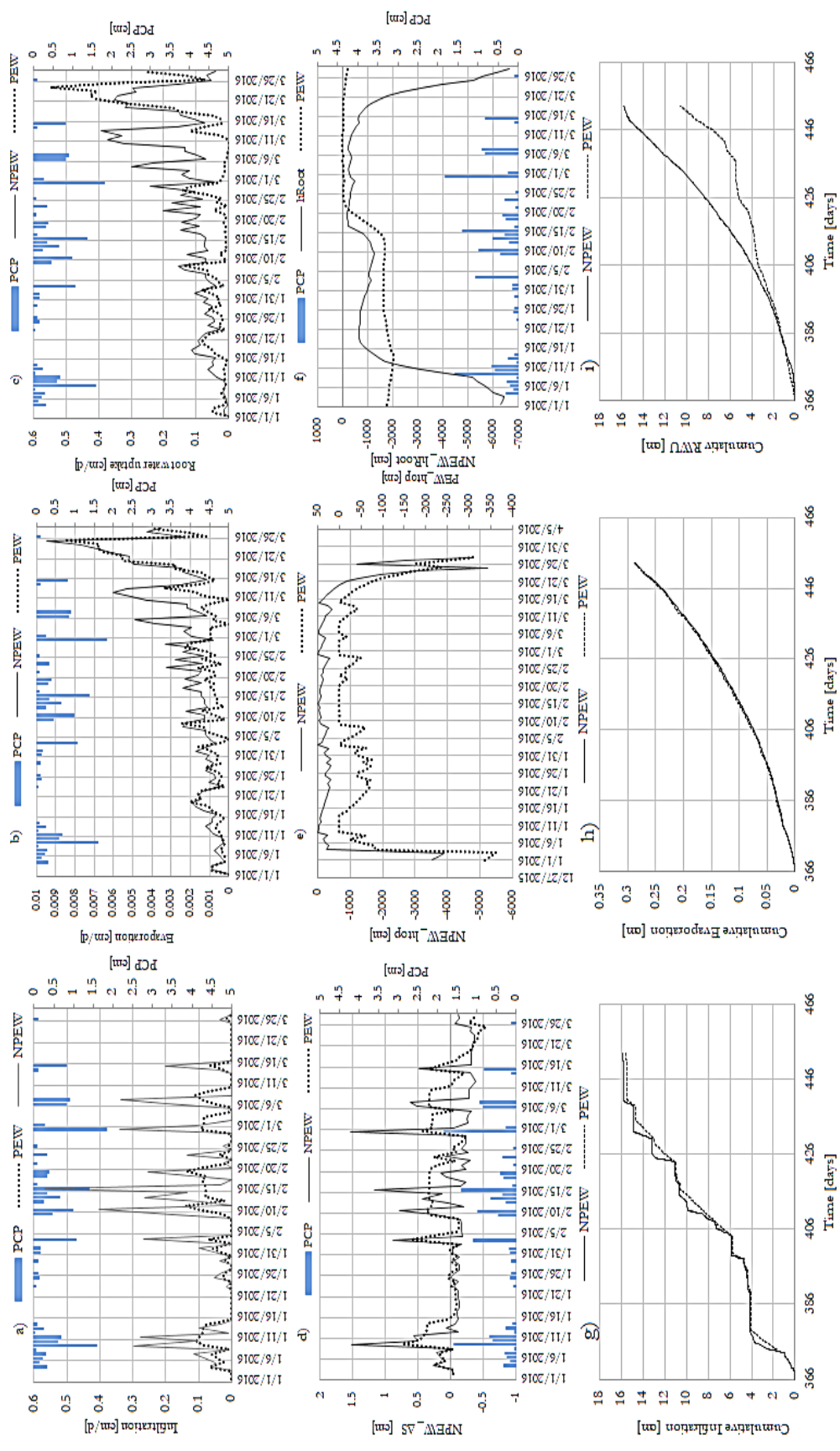
Figure 22: Comparison of HYDRUS simulated fluxes in PEW and NPEW site (January-March 2016) a) Actual surface flux (cm/d) b) Evaporation from soil (cm/d) c) Root water uptake from plant (cm/d) d) Changes in soil water storage e) head distribution in top layer and f) Root pressure head [cm] g) Cumulative infiltration (cm) f) Cumulative evaporation (cm) g) Cumulative Root water uptake (cm)

5.3.3. Validation with satellite data

Figure 21a compares the timing of ponding detected by satellite images (in plot 1) with respect to the HYDRUS simulated results. The dots presented in the figure represents the time period of satellite overpass used for mapping of PEW. The red dot indicates the time period when ponding was not detected in the satellite image, while the black dot indicates the ponding detected by satellite. A comparison was also made based on the number hits and missed events (Table 12). The number of hits indicated complete match between satellite detected and modelled ponding outputs. On the other hand missed represented satellite detected but not simulated by the model. Overall 14 images used for mapping showed PEW detection in all images except in 1/4/2016, 1/28/2016 and 3/11/2016 (Figure 11). The model simulated and the satellite detected ponding showed strong coherence, which is indicated by 10 hits (71 %) and 4 miss (29 %). However, the extent of ponding differed in the different time period. The extent of ponding detected ranged from 0.0001-0.0045 km² with an average area of 0.0015 km². Large extent (0.0045 km²) was measured during mid-February that shrunked to as low as 0.0011 km² by the end of the month. This increased extent of inundation correlated with the higher number of rainy days measured during the month (Table11). Additionally, it also corresponded to the simulated head of the mode. When the ponding extent was large, ponding head generated by the model also peaked. The model also resembled to the timing of ponding detected except at the end of February.

During January, ponding only started after continuous 5 rainy days followed by an intense rain of (15.9 mm) that triggered the accumulation at the surface. The model simulated ponding lasted for six days, but on satellite 2 days of ponding was observed. Satellite-detected ponding after 16th March was not simulated by the model. The possible reason for the differences can be explained by the fact that ponding in the area occurs in depression that accumulate water runoff from surrounding. But the model was only calibrated on one dimension where the possible lateral flow from the surrounding topography was not modelled. On the other hand errors from satellite data could also be introduced when the threshold used is difficult to separate saturated soil data with excess water in the area, the might overestimate the extent of PEW. Despite the low temporal frequency of the satellite data (5 or 7days), the model predicted timing and duration of ponding was in correspondence to the satellite data.

Table 12: Extent of ponding in plot 1

Satellite overpass	PEW area [km²]	Total % [km²]	Hit =1 Missed=0	Ponding depth*[cm]	Satellite overpass	PEW area	Total %	Hit =1 Missed=0	Ponding depth* [cm
1/4/2016	0	0	1	0	2/21/2016	0.0026	2.26	1	64
1/11/2016	0.0046	3.98	1	73	2/28/2016	0.0011	0.92	0	61
1/15/2016	0.0010	0.86	1	60	3/4/2016	0.0025	2.14	1	64
1/23/2016	0.0022	1.96	0	39	3/11/2016	0.0001	0.06	1	0
1/28/2016	0	0	1	0	3/16/2016	0.0013	1.10	1	67
2/9/2016	0.0008	0.73	1	75	3/23/2016	0.0007	0.61	0	63
2/16/2016	0.0046	3.91	1	65	3/28/2016	0.0003	0.24	0	28
*Depth estimated from drone based DEM and satellite derived binary images of ponding									
Total area of plot 1 = 0.114 km²									

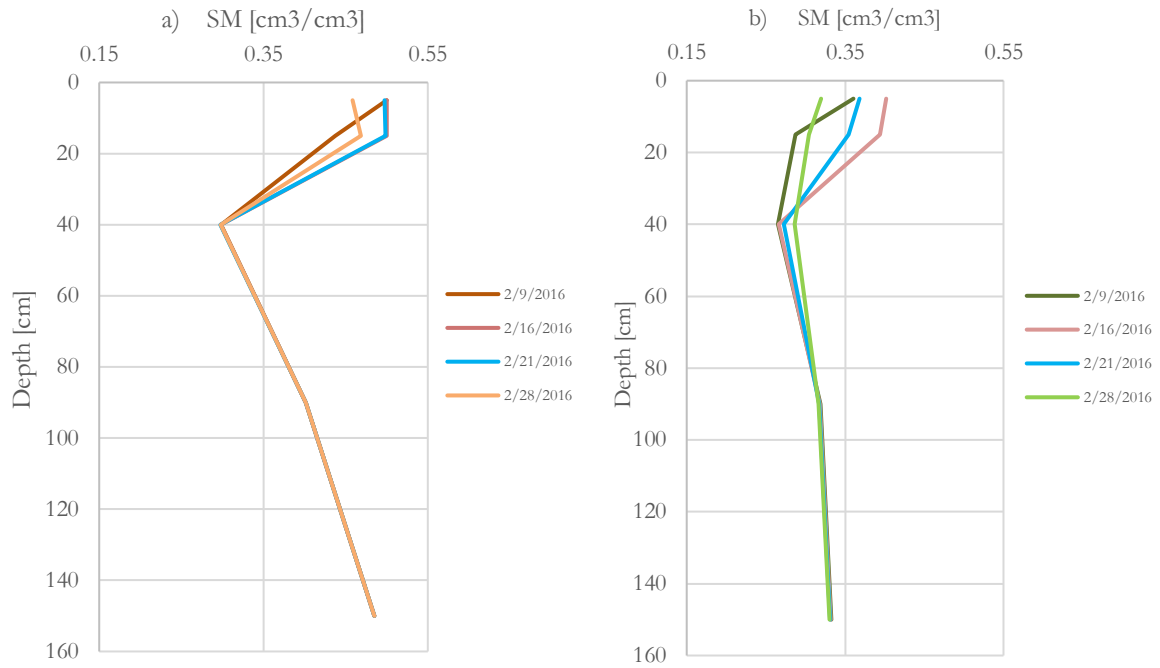## 5.3.4. Wetting process in response to satellite data

Figure 23: Wetting process measured at given time period

Water infiltrating into a dry soil, known as wet front, shows a distinct boundary between the upper wet part and lower dry part of the soil (Kirkham, 2005). Figure 23 shows the variability of soil water content within the soil profile. Comparison was made between the ponding conditions detected by satellite and the model output. It represents the dry and wet conditions measured through the profile during February. It showed two distinct pattern of wetting. In the PEW site, broader and shallower wetting fonts were noticed while in NPEW site smoother movement was observed. During first day of ponding (9th, February) the SWC was 0.50 cm³/cm³ which dropped to 0.4587 cm³/cm³ by the end of ponding period (28th February). During ponding, saturation was also attained till 15 cm and then the wetting font declined rapidly till 40 cm. This quick depletion can be attributed to evaporative fluxes. Sharp decline of wetting pattern showed the effect of inter clay layer impeding the transport of water in deeper profile. On the contrary, with the same magnitude of rainfall in NPEW site at a same depth, the wetting process was much narrower and deeper. This is because the presence of comparatively coarser layer in NPEW site than in PEW site. Shallow wetting depth and wider wetted width are reported as characteristics of clay soils that have more micropores per unit volume (Chikezie, Adedeji, & Isikwue, 2018). The simulated water content in PEW after 40 cm showed increasing values. This could be related to the capillary rise of water in the measured profile.

5.3.5. Runoff simulation in NPEW site

Case 2a: Simulation in the year 2015 to 2016 (25th Sep to 28th Mar) in NPEW location

Simulation in NPEW was carried out based on same time variable atmospheric boundary condition but with surface runoff condition and free bottom boundary condition, and also with changes in soil properties as measured in the site (Table 8). Runoff generation is influenced by the distribution and duration of intense rain and water content in the soil profile (Tan et al., 2018). "If the potential rate of infiltration exceeds the infiltration capacity of the soil, part of the water runs off, since the actual flux through the top layer is limited by moisture conditions in the soil" (Feddes, *et al.* 1988). It was implicitly considered that the site was slightly tilted for the water to flow as soon as it accumulated on the surface. The dry period of 2015 was considered as warmup period and 2016 (January to March) was used for analysis. Figure 24 shows the SWC profiles simulated for different days at different depths. The hydraulic conductivity of the top two layer was comparatively larger (7.15, 6.69 cm/d) than estimated in PEW site (1.48, 0.3 cm/d). Because of different nature of soils in the site and a bit higher K_{sat} value, very less saturation was reached in the modelled time period and thus very little runoff was generated. The average water that runs off was very less of 0.000155 cm/d with maximum measured as 0.004597cm/d (Figure 24). More runoff was generated during February (av. 0.0025 cm/d) which corresponded to the high rainfall measured during the period.
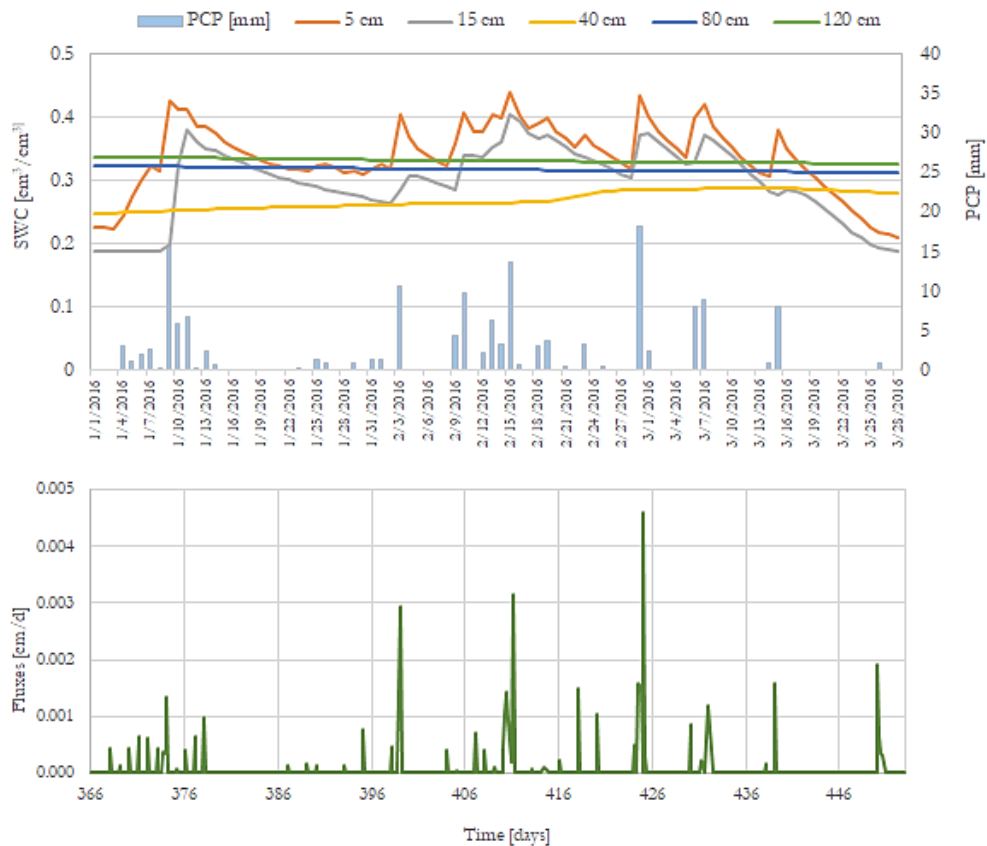
Figure 24: Time series of predicted SWC content (a, cm³/cm³) and runoff (b, cm/d) simulated in NPEW for the period of January to March 2016

Comparatively, the infiltration amount was greater in NPEW site than in PEW site (Figure 21a). The average rate of infiltration was measured as 0.059 cm/d, which was 54% higher than in PEW area. The cumulative plots of RWU (Figure 22i) showed that the rate of RWU from plants in NPEW site was much larger than in PEW. Almost 99.5% of the infiltration amount was taken up by the roots (Table 13). Soil water in deep layer would flow upward by the potential difference, when there is intense ET and eventually water would

be lost through ET (Liu, Lai, & Luo, 2015). Since actual evapotranspiration is the function of available water content in soil profile, increased infiltration in NPEW site increased the available water content and as a result, RWU was increased. In NPEW, the storage change is comparatively less (-2 cm) than in PEW, which accounted to 12.61% of infiltration amount. Negative storage change value also showed that the losses terms were larger than the input flux. All infiltrated water was almost transpired by plants. Plants under stress condition was much higher at the start (January) and end (February) of the study period (Figure 22f). The root zone pressure head was as low as -6633.40 cm which was close to wilting point (<-8000 cm). RWU was however under optimal condition (-25 to 1500) between mid-January to mid-March. On the other hand, in the PEW area, because the area was mostly under saturated condition, less stress was experienced by plants with a lowest pressure of -2045.30 cm. According to Feddes et al (1978), RWU ceases when close to saturation point of -10 cm. Such condition was measured during 4th to 11th of March in PEW site, which was also indicated by a flat line during the period in Figure 22f. RWU was observed to be in optimum condition during mid-February to end of March. In the NPEW site, the bottom flux was measured to be negative throughout the study period but an increasing tendency was noticed. This indicated that the incoming precipitation had negligible effect on the bottom flux. According to Tan et *al.*, (2018) using high intital value of soil water content can have many consequences such as: decrease in time of runoff as soil quickly saturates with high intial water content, decrease in depth of wetting, slow transport of infiltrated water due to decrease in pressure head gradient in soil profile that decreases the infiltration capacity of soil. Due to the error in the in situ SWC measurement in the NPEW site, the simulated SWC content could not be validated and subsequently the impact of initial values could not be assessed.

Though it was possible to simulate HYDRUS model based on the short time period of observed soil water content from the field, the amount of runoff generated and accumulation of water modelled was very less. The major limitation of the modelling in this study is that it was carried out only at a pixel level and the effect of topography was not modelled in the site. Therefore, the total amount of water running form the surrounding catchment to the discharge or the depression area could not be estimated.

Table 13: Water balance components

		PCP	Storage	E	T	Bot. flux	Runoff	WB
PEW		15.87	5.05	0.29	10.553	0	0	5.027
	%		31.82	1.83	66.50			
NPEW		15.87	-2.001	0.29	15.793	-1.788	0.006	-2.00
	%		-12.61	1.81	99.51	11.27	0.04	

6. CONCLUSION AND RECOMMENDATION

6.1. Conclusion

The objective of the present research was to understand the infiltration dynamics using HYDRUS-1D model in ponding and non-ponding location having different properties of soil. The measured soil physical parameters were able to identify the differences in properties of soil in regularly and non-regularly inundated areas. Soil physical parameters were found to play a major role in the formation of ponding in the area. It was evident that the particle size in ponding areas (PEW in plot 1 and bore 1 in plot 2) have heavy clay proportions to deeper layers than in non-ponding areas. The non-ponding area was primarily characterized by silty clay layer. Poor spatial prediction of particle size composition and texture was noted in soil grids database, which shows clay loam in all compared plots and corresponding depths. Measured BD and porosity was also highest in PEW site than in NPEW site. BD increased with depth and had inverse relationship with porosity. Low OM content was measured in both sites but higher proportion was noted in NPEW (2.5-8.8%). The measured soil parameters were used to generate soil hydraulic parameters using an indirect method.

Soil water infiltration process was studied by setting a 1D HYDRUS model with measured soil parameters of the PEW and NPEW sites. Model was calibrated based on field measurement of water content data for a shorter duration of 25th Sept- 5th December 2018. The simulated water content data during calibration showed a reasonable degree of match with the measured ones despite the error created by experimental setup. Lower accuracy was mainly achieved for the top layer which was more subjected to error created by extra cover layer added on the top of the soil profile. The average ME, MAE, RMSE, d-index and RVE in PEW was 0.006 cm³/cm³, 0.018 cm³/cm³, 0.018 cm³/cm³, 0.638, and -2.286 % respectively. This calibrated model was further applied to simulate ponding in the experimental sites (January to March 2016) corresponding to the excess water mapping carried out based on Sentinel images.

The results of simulation in two different sites showed different characteristics. HYDRUS 1D model was able to simulate ponding in the area which was frequently inundated. The timing of the ponding simulated by the model overlapped with the ponding mapped by the satellite images in overall. Despite the low temporal resolution of satellite image, the longer duration of ponding identified from the images was well simulated by the model. Quicker saturation of surface layer and thick clay layer underneath was found to control the downward transport of water. Heavy rain induced ponding in the area was able to retain water in such condition till 12 days in February. Ponding simulated by the model was also observed to last for 1, 2, 5, and 6 days over the study period. During the ponding period, it was through ET that most of water was lost rather than through infiltration. The infiltration rate modelled was half times slower in PEW (0.032 cm/d) site than in NPEW site (0.059 cm/d) which can be attributed to the fine clay layer deposited till one meter.

HYDRUS model developed in the study site was capable of simulating ponding timing and duration. The simulated depths of ponding was however very little (0.27-1.22 cm) compared to depths estimated from drone based DEM (28-75 cm). The outputs suggested further need of calibration of the model, where the infiltration was still found to be overestimated by the model. Also, the runoff generated was much lower in NPEW (av. 0.0025cm/d) than what would be realistic.

With a detailed soil map of the area, a high-resolution DEM and good quality of meteorological inputs it is possible to predict with modelling the occurrence of ponding, the timing, duration and extent of inundation. Also with satellite derived inundation images combined with high resolution DEM could be useful to define

the time series of inundation depth. This data could also be useful for calibration in absence of field measurement. Based on SPP measurement and modelling outputs, it can also be concluded that the excess water formation in the PEW area was mainly accumulative.

Though the model was able to predict ponding in the area, its accuracy highly relies on the quality of the input data set such as hydraulic conductivity and water retention parameters. Further calibration is required to assess the accuracy of the infiltration or the volume of ponding measured. The measured water content data from sensors installed at different depths under ponding condition could be useful to increase the accuracy of the model and thus better prediction. Since the spatial variability of soil properties is very high, the measured parameters needs to be verified and updated with locally available datasets in the region. It is also noteworthy that the area is exposed to heavy snowfall during winter. Frozen soil in winter could also impede water flow in subsurface layer. Effect of frozen soil combined with rainfall on soil water infiltration could provide new insight on soil water interaction in the ponding areas.

6.2.   Recommendations

- The study was analyzed only at a pixel level. A better calibrated model can be prepared considering the actual crop growth parameters over simulation period of interest. Also, it was evident from the field that ponding occurred in natural depression but the influence of surrounding topography on ponding can be further studied using 2D or 3D models.
- The soil is exposed to frequent seasonal process of wetting and drying and with the nature of swelling observed in the region, the effect of hysteresis on soil water movement need to be further studied.
- Sensitivity of the model to the measured soil hydraulic parameters need to be tested to understand its influence.
- It is clear that particle size composition in the inundated areas are different than the non-inundated areas and that they play a key role in development of PEW. Gridded database like Soil Grids needs to be improved to better understand the soil water transport dynamics in the inundated areas.
- A ponding excess water hazard map can be projected based on mapping regularly inundated areas by satellite images and combing them with the soil water infiltration model.

REFERENCES

Adamcova, R., Ottner, F., Durn, G., Greifeneder, S., Dananaj, I., Dubikova, M., … Kapelj, S. (2005). Problems of Hydraulic Conductivity Estimation in Clayey Karst Soils Geologia Croatica Problems of Hydraulic Conductivity Estimation in Clayey Karst Soils. *Geologia Croatica*, *58*(May 2014), 198–203. https://doi.org/10.4154/GC.2005.11

Allen, R. G., Pereira, L. S., Raes, D., & Smith, M. (1998). *Crop Evapotranspiration*. Rome: Food and Agriculture Organization of the United Nations. Retrieved from http://www.fao.org/docrep/X0490E/x0490e00.htm#Contents

Barreto, S., Bártfai, B., Engloner, A., Liptay, Á. Z., Madarász, T., & Vargha, M. (2017). *Water in Hungary*. Budapest. Retrieved from http://mta.hu/data/dokumentumok/Viztudomanyi Program/Water_in_Hungary_2017_07_20.pdf

Barta, K. (2013). Inland excess water projections based on meteorological and pedological monitoring data on a study area located in the Southern part of the Great Hungarian Plain. *Journal of Environmental Geography*, *6*(3–4), 31–37. https://doi.org/10.2478/jengeo-2013-0004

Barta, K., Bata, T., Benhhe, B., & Miograd, B. et al. (2013). *Inland Excess Water*. Szeged and Novi Sad. Retrieved from http://jlevente.com/publications/SzatmariVanLeeuwen_Inland_Excess_Water.pdf

Bioresita, F., Puissant, A., Stumpf, A., & Malet, J. P. (2018). A method for automatic and rapid mapping of water surfaces from Sentinel-1 imagery. *Remote Sensing*, *10*(2). https://doi.org/10.3390/rs10020217

Bot, A., & Benites, J. (2005). *The Importance of Soil Organic Matter*. Rome, Italy.

Bozán, C., Körösparti, J., Pásztor, L., Kuti, L., Kozák, P., & Pálfai, I. (2009). Gis-based mapping of excess water inundation hazard in Csongrád county (Hungary). *Analele Universităţii Din Oradea*, *XIV*(2000), 678–684.

Bozán, C., Körösparti, J., Pásztor, L., Kuti, L., & Pálfai, I. (2008). Mapping of excess water hazard in the region of South Hungarian Great Plain. *XXIVth Conference of the Danubian Countries on the Hydrological Bases of Water Management*.

Bozán, C., Körösparti, J., Pásztor, L., & Pálfai, I. (2013). Excess water hazard mapping on the South Great Hungarian Plain. *13th International Conference on Environmental Science and Technology (CEST)*, (September), 5–7.

Brisco, B. (2015). Mapping and Monitoring Surface Water and Wetlands with Synthetic Aperture Radar. *Remote Sensing of Wetlands: Applications and Advances*, (August), 119–136. https://doi.org/10.1201/b18210-9

Chaudhari, P. R., Ahire, D. V, Ahire, V. D., Chkravarty, M., & Maity, S. (2013). Soil Bulk Density as related to Soil Texture , Organic Matter Content and available total Nutrients of. *International Journal of Scientific and Research Publications*, *3*(2), 1–8. Retrieved from http://www.ijsrp.org/research-paper-0213/ijsrp-p1439.pdf

Chikezie, A. ., Adedeji, M. A., & Isikwue, M. O. (2018). Prediction of soil wetting pattern for three soil types under drip irrigation. *International Journal of Agriculture and Environmental Research*, *4*(10), 1–18.

Connolly, R. . (1998). Modelling effects of soil structure on the water balance of soil–crop systems: a review. *Soil and Tillage Research*, *48*(1–2), 1–19. https://doi.org/10.1016/S0167-1987(98)00128-7

Cosby, B. J., Hornberger, G. M., Clapp, R. B., & Ginn, T. R. (1984). Exploration of the Relationships of Soil Moisture Characteristics to the Physical Properties of Soils. *Water Resources Research*, *20*(6), 682–690. https://doi.org///doi.org/10.1029/WR020i006p00682

Csendes, B., & Mucsi, L. (2016). Inland excess water mapping using hyperspectral imagery. *Geographica Pannonica*, *20*(4), 191–196. https://doi.org/10.18421/GP20.04-01

Eijkelkamp Soil and Water. (2017). *Laboratory permeameters*. The Netherlands.

Emilio, A. D., Aiello, R., Consoli, S., Vanella, D., & Iovino, M. (2018). Artificial Neural Networks for Predicting the Water Retention Curve of Sicilian Agricultural Soils. *Water*, *10*(1431), 1–13. https://doi.org/10.3390/w10101431

Faragó, T., Láng, I., & Csete, L. (2010). *Climate change and Hungary : Mitigating the hazard and preparing. VAHAVA Report.* Retrieved from http://www.vahavahalozat.hu/files/vahava-2010-12-korrigalt-2.pdf

Feddes, R. A., Kabat, P., Van Bakel, P. J. T., Bronswijk, J. J. B., & Halbertsma, J. (1988). Modelling soil water dynamics in the unsaturated zone — State of the art. *Journal of Hydrology*, *100*(1–3), 69–111. https://doi.org/10.1016/0022-1694(88)90182-5

Feddes, R. A., Kowalik, P., Kolinska-Malinka, K., & Zaradny, H. (1976). Simulation of Field Water Uptake by Plants using a Soil Water Dependent Root Extraction Function. *Journal of Hydrology*, *31*(1–2), 13–26. https://doi.org/10.1016/0022-1694(76)90017-2

Gál, N., & Farsang, A. (2013). Weather Extremities and Soil Processes: Impact of Excess Water on Soil Structure in the Southern Great Hungarian Plain. In D. Loczy (Ed.), *Geomorphological impacts of extreme weather: Case studies from central and eastern Europe* (pp. 313–325). Dordrecht: Springer Netherlands. https://doi.org/10.1007/978-94-007-6301-2

Gál, N., Tóth, T. M., Raucsik, B., Földes, T., & Farsang, A. (2017). Effects of inland excess water on bulk density and clay mineralogy of a chernozem soil using xrct and xrpd techniques. *Carpathian Journal of Earth and Environmental Sciences*, *12*(1), 189–196.

Giordan, D., Notti, D., Villa, A., Zucca, F., Calò, F., Pepe, A., … Allasia, P. (2018). Low cost, multiscale and multi-sensor application for flooded area mapping. *Natural Hazards and Earth System Sciences*, *18*(5), 1493–1516. https://doi.org/10.5194/nhess-18-1493-2018

Greve, A., Andersen, M. S., & Acworth, R. I. (2010). Investigations of soil cracking and preferential flow in a weighing lysimeter filled with cracking clay soil. *Journal of Hydrology*, *393*(1–2), 105–113. https://doi.org/10.1016/j.jhydrol.2010.03.007

Gundalia, M. (2018). Estimation of infiltration rate based on complementary error function peak for Ozat watershed in Gujarat (India), *2*(3), 289–294. https://doi.org/10.15406/ijh.2018.02.00083

Haghnazari, F., Shahgholi, H., & Feizi, M. (2015). Factors affecting the infiltration of agricultural soils : review. *International Journal of Agronomy and Agricultural Research*, *6*(5), 21–35. Retrieved from https://pdfs.semanticscholar.org/1263/7df77243763c7499bad3e843905b31e03835.pdf

Hillel, D. (2003). *Introduction to environmental soil physics.* Academic Press. https://doi.org/https://doi.org/10.1016/B978-0-12-348655-4.X5000-X

Horváth, Á., Ács, F., & Breuer, H. (2009). On the Relationship Between Soil, Vegetation and Severe Convective Storms: Hungarian case studies. *Atmospheric Research*, *93*(1–3), 66–81. https://doi.org/10.1016/j.atmosres.2008.10.007

Huang, W., DeVries, B., Huang, C., Lang, M., Jones, J., Creed, I., & Carroll, M. (2018). Automated Extraction of Surface Water Extent from Sentinel-1 Data. *Remote Sensing*, *10*(5), 797. https://doi.org/10.3390/rs10050797

Jana, R. B., Mohanty, B. P., & Springer, E. P. (2007). Multiscale Pedotransfer Functions for Soil Water Retention. *Vadose Zone Journal*, *6*, 868–878. https://doi.org/10.2136/vzj2007.0055

Kacimov, a. R., Al-Ismaily, S., & Al-Maktoumi, a. (2010). Green-Ampt One-Dimensional Infiltration from a Ponded Surface into a Heterogeneous Soil. *Journal of Irrigation and Drainage Engineering*, *136*(1), 68–72. https://doi.org/10.1061/(ASCE)IR.1943-4774.0000121

Kirkham, M. B. (2005). *Principles of soil and plant water relations.* Boston: Academic Press. Retrieved from http://www.esalq.usp.br/lepse/imgs/conteudo_thumb/Principles-of-Soil-and-Plant-Water-Relations-by-M-B--Kirkham--2005-.pdf

Kozma, Z. (2013). *Development of the Risk Based Evaluation and Modeling Methodology of Excess Water Extremiteis.* PhD thesis, Budapest University of Technology and Economics, Budapest.

Kuti, L., Kerék, B., & Vatai, J. (2006). Problem and prognosis of excess water. *Carpathian Journal of Earth and Environmental Sciences*, *1*(1), 5–18. Retrieved from http://www.ubm.ro/sites/CJEES/upload/2006_1/Kuti.pdf

Leeuwen, B. Van, & Tobak, Z. (2014). Operational Identification of Inland Excess Water Floods Using

Satellite Imagery. *GI_Forum 2014 – Geospatial Innovation for Society*, (August), 12–15. https://doi.org/10.1553/giscience2014s12.Operational

Liu, T., Lai, J., & Luo, Y. (2015). Study on extinction depth and steady water storage in root zone based on lysimeter experiment and HYDRUS-1D simulation. *Hydrology Researech*, *46*(January), 871–879. https://doi.org/10.2166/nh.2015.191

Mezősi, G. (2017). *The Physical Geography of Hungary*. Cham: Springer. https://doi.org/10.1007/978-3-319-45183-1

Nemes, A., Rawls, W. J., & Pachepsky, Y. A. (2005). Influence of Organic Matter on the Estimation of Saturated Hydraulic Conductivity. *Soil Science Society of America Journal*, *69*(4), 1330. https://doi.org/10.2136/sssaj2004.0055

Pásztor, L., Körösparti, J., Bozán, C., Laborczi, A., & Takács, K. (2015). Spatial risk assessment of hydrological extremities: Inland excess water hazard, Szabolcs-Szatmár-Bereg County, Hungary. *Journal of Maps*, *11*(4), 636–644. https://doi.org/10.1080/17445647.2014.954647

Pásztor, L., Pálfai, I., Bozán, C., János, K., Szabó, J., Bakacsi, Z., & Kuti, L. (2006a). Spatial stochastic modelling of inland inundation hazard. In *9th AGILE Conference on Geographic Information Science* (pp. 139–143).

Pásztor, L., Pálfai, I., Bozán, C., János, K., Szabó, J., Bakacsi, Z., & Kuti, L. (2006b). Spatial stochastic modelling of inland inundation hazard. *9th AGILE Conference on Geographic Information Science*, 139–143.

Perfect, E. (2003). A Pedotransfer Function for Predicting Solute Dispersivity: Model Testing and Upscaling. In Y. Pachepsky, D. E. Radcliffe, & M. H. SelimSelim (Eds.), *Scaling Methods in Soil Physics*. (pp. 89–96). Boca Raton, Florida: CRC Press. https://doi.org/10.1201/9780203011065

Rawls, W. J., Brakensiek, D. L., & Saxton, K. E. (1982). Estimation of Soil Water Properties. *Transactions of the ASABE*, *25*(5), 1316–1320. https://doi.org/10.13031/2013.33720

Rientjes, T. (2015). *Hydrologic Modelling for Intergated Water Resource Assessments*. Faculty of geo-Information Science and Earth Observation, University of Twente. Enschede.

Schaap, M. G., Leij, F. J., & Genuchten, M. T. Van. (2001). Rosetta : A Computer Program for Estimating Soil Hydraulic Parameters with Hierarchical Pedotransfer Functions. *Journal of Hydrology*, *251*, 163–176. https://doi.org/10.1016/S0022-1694(01)00466-8

Šimůnek, J, van Genuchten M. Th., Šejna, M. (2012). Hydrus: Model Use, Calibration, and Validation. *Transactions of the ASABE*, *55*(1987), 1261–1274. https://doi.org/10.13031/2013.42239

Šimůnek, J., Šejna, M., Saito, H., Sakai, M., & van Genuchten, M. T. (2013). *The HYDRUS-1D Software Package for Simulating the One-Dimensional Movement of Water , Heat , and Multiple Solutes in Variably-Saturated Media :* California: University of California Riverside.

Tan, J., Song, H., Zhang, H., Zhu, Q., Xing, Y., & Zhang, J. (2018). Numerical investigation on infiltration and runoff in unsaturated soils with unsteady rainfall intensity. *Water*, *10*(914), 1–16. https://doi.org/10.3390/w10070914

Tanveera, A., Kanth, T. A., Tali, P. A., & Naikoo, M. (2016). Relation of Soil bulk Density with Texture , Total organic matter content and Porosity in the Soils of Kandi Area of Kashmir valley , India. *International Research Journal of Earth Sciences*, *4*(1), 1–6. https://doi.org/http://www.isca.in/EARTH_SCI/Arch

Van Genuchten, M. (1980). A Closed-form Equation for Predicting the Hydraulic Conductivity of Unsaturated Soils1. *Soil Science Society of America Journal*, *44*(September 1980), 892–898. https://doi.org/10.2136/sssaj1980.03615995004400050002x

van Leeuwen, B. (2012). *Artificial neural networks and geographic information systems for inland excess water classification*. PhD Thesis, University of Szeged.

van Leeuwen, B., Pravetz, T., Liptay, Z. A., & Tobak, Z. (2016). Physically Based Hydrological Modelling of Inland Excess Water. *Carpathian Journal of Earth and Environmental Sciences*, *11*(2), 497–510.

van Leeuwen, B., Tobak, Z., Kovács, F., & Sipos, G. (2017). Towards a continuous inland excess water flood monitoring system based on remote sensing data. *Journal of Environmental Geography*, *10*(3–4), 9–

15. https://doi.org/10.1515/jengeo-2017-0008

van Reeuwijk, L. P. (2002). *Procedures for soil analysis*. Wageningen . Retrieved from www.isric.org

Vereecken, H., & Feyen, J. (1989). Estimating the Soil Moisture Retention Characteristic From Texture , Bulk Density , and Carbon Content. *Soil Science*, *148*(February 2019), 389–403. https://doi.org/10.1097/00010694-198912000-00001

Wang, S. Q., Song, X. F., Wei, S. C., & Shao, J. L. (2016). Application of HYDRUS-1D in understanding soil water movement at two typical sites in the North China Plain. *Journal of Groundwater Science and Engineering*, *4*(1), 1–11. Retrieved from

http://gwse.iheg.org.cn/EN/article/downloadArticleFile.do?attachType=PDF&id=204

Weil, R. R., & Brady, N. C. (2016). *The Nature and Properites of Soil* (15th ed.). Columbus: Pearson. Retrieved from https://www.researchgate.net/publication/301200878_The_Nature_and_Properties_of_Soils_15th _edition

Willmott, C. J., Ackleson, S. G., Davis, R. E., Feddema, J. J., Klink, K. M., Legates, D. R., … Rowe, C. M. (1985). Statistics for the Evaluation and Comparison of Models. *Journal of Geophysical Research*, *90*(5), 8995–9005. https://doi.org/10.1029/JC090iC05p08995

Wosten, J. H. M., Lilly, A., Nemes, A., & Le Bas, C. (1999). Development and use of a database of hydraulic properties of European soils. *Geoderma*, *90*(3–4), 169–185. https://doi.org/10.1016/S0016-7061(98)00132-3

Wösten, J. H. M., Pachepsky, Y. A., & Rawls, W. J. (2001). Pedotransfer functions: Bridging the gap between available basic soil data and missing soil hydraulic characteristics. *Journal of Hydrology*, *251*(3–4), 123–150. https://doi.org/10.1016/S0022-1694(01)00464-4

Yun, Q. (2017). *Ponding Excess Water Mapping in Agricultural Areas in Hungary*. Universtiy of Twente, Faculty of Geoinformation Science and Earth Observation. Retrieved from https://webapps.itc.utwente.nl/librarywww/papers_2017/msc/wrem/qiu.pdf

Zheng, C., Lu, Y., Guo, X., Li, H., Sai, J., & Liu, X. (2017). Application of HYDRUS-1D model for research on irrigation infiltration characteristics in arid oasis of northwest China. *Environmental Earth Sciences*, *76*(23), 1–11. https://doi.org/10.1007/s12665-017-7151-2
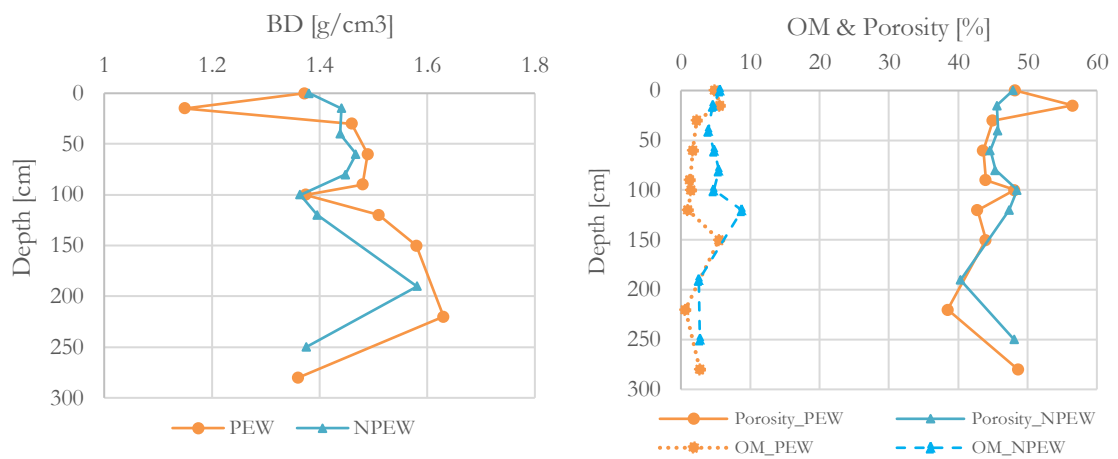
APPENDICES

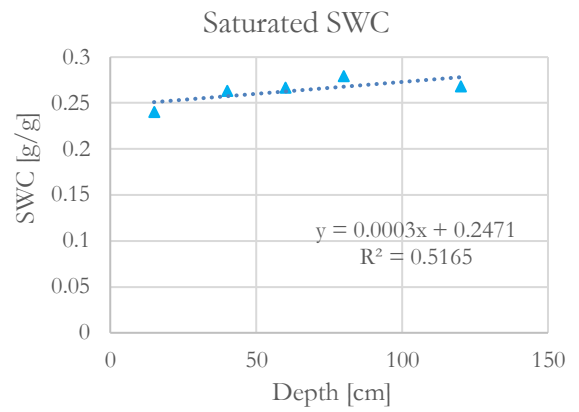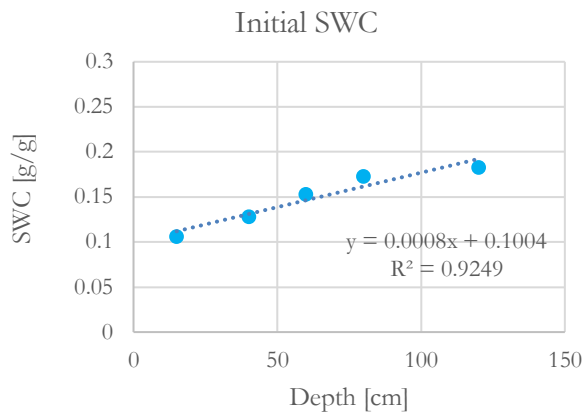Annex 1: Pipette analysis process (Oxidation process, Pipetting process, oven dried sample cups
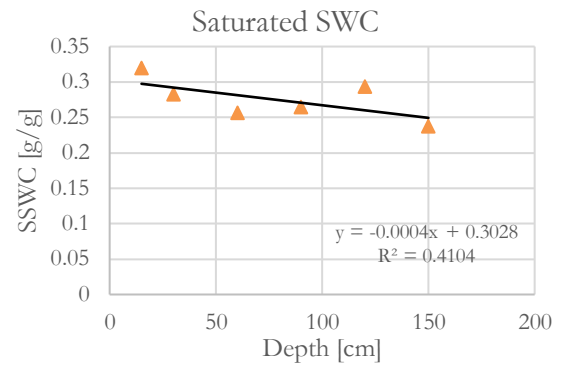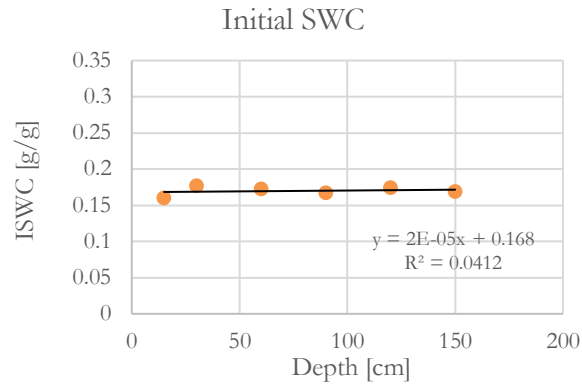

Annex 2: Hydraulic conductivity measurement using Permeameter

Annex 3: BD, Porosity & OM with respect to depth in PEW and NPEW

Annex 4: Initial and saturated water content measured based weight basis

Initial SWC

y = 2E-05x + 0.168
R² = 0.0412

Saturated SWC

y = -0.0004x + 0.3028
R² = 0.4104

Initial SWC

y = 0.0008x + 0.1004
R² = 0.9249

Saturated SWC

y = 0.0003x + 0.2471
R² = 0.5165

Annex 5: Box plot of SHP (PEW & NPEW)